Analysis of Liquid Atomization Using Ultrasonic Waves

A Major Qualifying Project

submitted to the faculty of

WORCESTER POLYTECHNIC INSTITUTE

in partial fulfilment of the requirements for the

degree of Bachelor of Science

By:

Matthew Wong

Date:

December 16, 2022

Report Submitted to:

Professor Adam C. Powell

Associate Professor

Mechanical Engineering

Table of Contents

Table of Figures

List of Tables

Abstract

Although the world is taking action to reduce its use of fossil fuels, current infrastructure still requir a combustion engine or liquid injection combustion unit to generate power. Thus, develop of new and improved methods of liquid fuel injection are warranted. One such technology is the approach of ultrasonic atomization. To study this phenomenon, a liquid droplet is dropped vertically towards a node of a generated standing wave. With further experimentation, it is possible to understand the variable factor and behavior of ultrasonic atomization to fine-tune the method for use of controlling mean atomization diameter, droplet diameter distribution, and droplet distribution density. Water sensitive paper was used to imprint the immediate droplet fragmentation, which is scanned digitally using an electronic microscope. Image processing program ImageJ is then used to threshold transform the picture and analyze the droplet count and individual area. Although experimentation and data collection were successful, the limited number of different tests compiled leaves the current understanding of the atomization behavior to be inconclusive. However, with retrial of testing conditions and the compilation of more test variables, we can stabilize observed correlations in the current comparison tests.

Acknowledgement

Chapter 1: Background

1. Introduction

Liquid fuel-based power generation, although detrimental in long-term use to our world environment, continues to be a vital source of energy for the world. According to the United States Energy Information Administration (EIA), as of the near future, the world's consumption of liquid fuels is expected to rise by 2.1 million barrels per day to 99.5 million total barrels a day through 2022 and forecasted to rise by about 1.5 million barrels per day in 2023 to 101.03 million total barrels a day. (U.S. Energy Information Administration (EIA), 2022) Out of the variety of generators for liquid fuels, internal combustion engines accounts for 23% of all fossil fuel use and 10% of the world's total greenhouse gas emission. (Dahham et al., 2022) In recent times, internal combustion engines have been deployed at an increasing pace as a means of emergency power, exceeding a total additional deployment worth threshold of 200 megawatts a year by 2000 and the 600 megawatts threshold by 2010. (U.S. Energy Information Administration (EIA), 2019) To counteract the growing greenhouse gas and global warming effects caused by the consistent need for liquid fuel power, the United States government is looking forward to push for a near or total net-zero greenhouse gas emission target by 2050. (Shields, 2021) However, current combustion engines are far from achieving this target. Although combustion engines in perfect thermodynamic settings can theoretically exceed 60 percent efficiency, the efficiency of current combustion engines only reach around 47.5 percent. (Haga, 2011) To ensure the longevity of combustion engines, they are becoming one of the main power generation candidates for technological research and improvements to reduce fuel use and reduce waste emission. One of such technological paths is in the application of the standing ultrasonic sound wave atomization phenomenon into combustion fuel injection.

Since 2019, Professor Hiroyasu Saito of Shibaura Institute of Technology (SIT) has been co-participating in a study of the characteristics of standing ultrasonic sound wave atomization on falling liquid droplets. The goal is to understand the influential factors and behaviors behind this atomization phenomena. The results will provide a better understanding and control for liquid atomization that can be implemented into combustion engines to improve combustion state modulation, such as the resulting combustion flame shape and temperature. (Toyota et al., 2019) In the same vein, the improved control in the liquid atomization process will also allow non-traditionally tuned liquid, such as in viscosity and density, to be optimally atomized for complete combustion. With this knowledge, thermal efficiencies for combustion engines and power generation systems can be improved while new, net-zero experimental combustive fuel sources can also be utilized with current combustion methods.

In addition, this phenomenon can also be applied in fields of research such as material analysis, industrial processes such as distillation, or common consumer products such as air ventilation systems. (Yang et al., 2020) The atomization principals of the standing ultrasonic wave can be applied to fragmentation of small solid materials. In the instance of research on melt atomization, Żrodowski and company were successful in atomizing spherical powders of novel alloys with little alteration to their properties and melt behavior while promoting crystallization bonding. (Żrodowski et al., 2021) This experimental processing method can provide faster development of experimental additive manufacturing alloys with improved and expanded characteristics yet don't carry required by performance-limiting character of traditional additive manufacturing alloys. Current additive manufacturing allows having high flowability at the cost of low ductility is a notable example.

The purpose of this research is to continue Professor Saito's study of standing ultrasonic sound wave atomization and succeed in improving the reproducibility of the experiments previously performed, to discover and record the behavioral characteristics due to the variable factors in the atomization experiment, and to integrate the current experimental process with other liquids and fuels.

2. Standing ultrasonic sound waves

2a. Definition of an ultrasonic sound wave

      Ultrasonic sound waves are high frequency vibrations that travel through excitation of

particles in a medium, such as solid materials or the air. Typically, frequencies deemed

ultrasonic exceed or are around 20 kilohertz, which just meet the upper limit of frequency that

humans can hear.

2b. Measurement factors and methods for ultrasonic sound waves

      Due to their high frequencies, ultrasonic wavelengths tend to be relatively shorter than

infrasonic wavelengths. This is due to the relationship between the velocity c [m/s], frequency f

[Hz], and wavelength λ [m] of a sound wave shown here in equation (1.2.1):

$$\lambda = c / f \tag{1.2.1}$$

The sound wave's velocity is dependent on the material it is passing through. In air, with relation

to the adiabatic index constant γ, the universal gas constant R [J /mol * K], the molecular mass of

air M [kg/mol], and the temperature of the air T [Kelvin], it is determined with this equation

(1.2.2):

$$c = \sqrt{(\gamma RT/M)} \tag{1.2.2}$$

Although the molecular mass of air might have a slight difference due to relative humidity in a

laboratory setting, along with the adiabatic index and the universal gas constant, the three values

are relatively stable constants within a laboratory setting. Thus, in a laboratory, the temperature

proves to have the most determinable effect on the resulting sound wave velocity and, in effect,

the resulting wavelength.

Sound waves themselves are generated from material capable of vibrating within a specific frequency, direction, and intensity. Usually, this is done with a transducer, a piezoelectric device capable of receiving an alternating current voltage signal and converting into physical vibrations. The transducer itself with expand and contract it's piezoelectric diaphragm to generate the waveform. For example, with the Langevin bolt-on transducer shown in Figure 1 below, the diaphragm requires longitudinal space to expand and contract as it generates the ultrasonic sound wave.
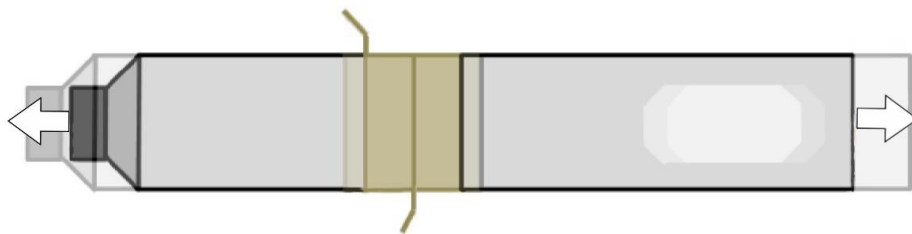
Figure 1. Langevin transducer expanding and contracting to generate ultrasonic sound wave

Attachments can be interfaced with the transducer to shape the vibration's output, either to oscillate a physical apparatus or to direct a sound wave. As so, transducers come in a variety of forms and arrangements.

2c. Generating standing wave with resonance

To generate an ultrasonic wave that is both strong and has a non-moving waveform to disrupt the liquid droplet consistently, the properties of acoustic resonance can be used as means of amplification and generation of a standing wave. By introducing a sound wave of similar frequency and amplitude in the opposite direction, once the phases match, the waves will

superimpose and sum the sound wave amplitudes and velocity, forming a stable wave with an increased amplitude. A standing wave can be characterized by points where the wave is not displacing and where the maximum amplitude is exerted. (University of Tennessee, n.d.) As seen in Figure 2 below, the points where the wave not displacing are called "Nodes" while the points where the wave reaches maximum amplitude are called "Antinodes".
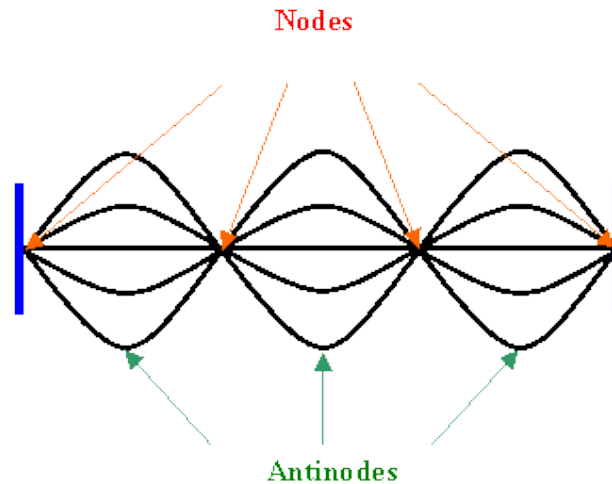
Figure 2. Graphical example of a standing wave. Reproduced from labman.phys.utk.edu

Either an opposite facing transducer or reflector can be used to send a opposite traveling wave towards the transducer and modulate with the actively generated wave. For a reflector setup, generated waves are outputted across a parallel, uniform surface equal or greater in reflecting surface area to the wave's directed surface area.

2d. Application for atomization

The standing wave produces a radiation force from two aspects, wave momentum and beam sound pressure. The generated and reflected beam carries two acoustical forces (Luo et al., 2017). Thus, at the node point, there are two directional pressures applied by the two neighboring, opposite moving, waveforms capable of compressing a medium. Depending on the

generated pressure, which can be recognized by measurement of its generated power, the wave

will be capable of fragmenting liquid droplets and solids into particles with differing levels of

fragment density, distribution, and range. This characteristic of an ultrasonic standing sound

wave is the fundamental method of atomization this research is seeking to further study.

3. Analysis methods of liquid atomization

3a. Definition of atomization

Atomization is the transformation of bulk liquid into an array of small particles referred

to as sprays. (Lefebvre & McDonell, 2017) The process begins with the development of

disturbances in a flow of liquid which separates the flow into ligaments and eventually into

drops, resulting in an output of spray.

3b. Measurement factors and methods for atomization

Initial density, surface tension, and viscosity of the liquid and the density, velocity,

distribution of the resulting drops being launched which affect the atomization process and

determines the characteristics of the resulting spray. (Lefebvre & McDonell, 2017) External

elements, such as those that construct the standing wave which crushes the droplet are also

important factors, which include sound pressure, standing wave power (a derivative of the sound

pressure), and sound frequency. By acquiring the liquid's surface tension, excitation frequency,

and the liquid's density, the median diameter of the atomization distribution can be calculated

with the following equation (1.3.1).

$$D = 0.34(8\pi T/\rho F^2)^{1/3} \tag{1.3.1}$$

This equation is synthesized by Lang from the observed proportionality of capillary wavelength and ultrasonic atomized droplet sizes. (Lang, 1962) In the equation, T is the surface tension of the liquid in Newton/Meters (N/m), ρ is the density of the liquid, F is the external excitation frequency in Hertz (hz), and D is the resulting median diameter of the atomization distribution. We can assume that the external excitation frequency, which is produced by the capillary waves in the liquid medium before fragmentation of the droplet, is equal to the frequency we are applying to the standing wave.

To record and measure these factors of atomization, there are an array of methods that are mechanical, electrical, and optical based. However, this paper will focus on the candidate optical and mechanical imaging techniques accessible within SIT's combustion laboratory, which include the following: laser diagnostics, high-speed photography, mechanical drop collection with water sensitive paper, and image analysis software ImageJ.

3c. Optical imaging: laser diagnostics

Laser diagnostics consist of a light source, usually a laser, passing through lenses and mirrors to concentrate and illuminate a thin plane of a medium. The medium which it illuminates will be tagged with either a separate fluorescent material or by the laser itself. Detectors will be arranged to analyze the output laser to detect for illumination of mediums through laser wavelength disruption. Once detected, an optical camera, captures the illuminated medium. (Xing et al., 2016)

Although many methods are developed, there are only a certain amount of laser diagnostics systems that have been practically applied to research and can be commercially

purchased. These include the planar laser-induced fluorescence (PLIF) system and the tunable

diode laser absorption spectroscopy (TDLAS) system. (Xing et al., 2016)

The PLIF system consists of a laser light source, lenses arrangement, fluorescent

element, and optical system for recording results, as seen in Figure 3 below. Operation of the

PLIF system comprises of the laser output being translated to a sheet by the lens arrangement,

which and illuminates the testing medium. To make sure the medium is detectable, a fluorescent

element is integrated into the medium during testing. Once the laser reaches the medium, the

fluorescent elements is excited and releases photon energy. The optical systems, a PLIF signal

camera and a particle image velocimetry (PIV) camera, are then able to take measurements of the

emitted wavelength to determine the concentration and velocity of the medium.
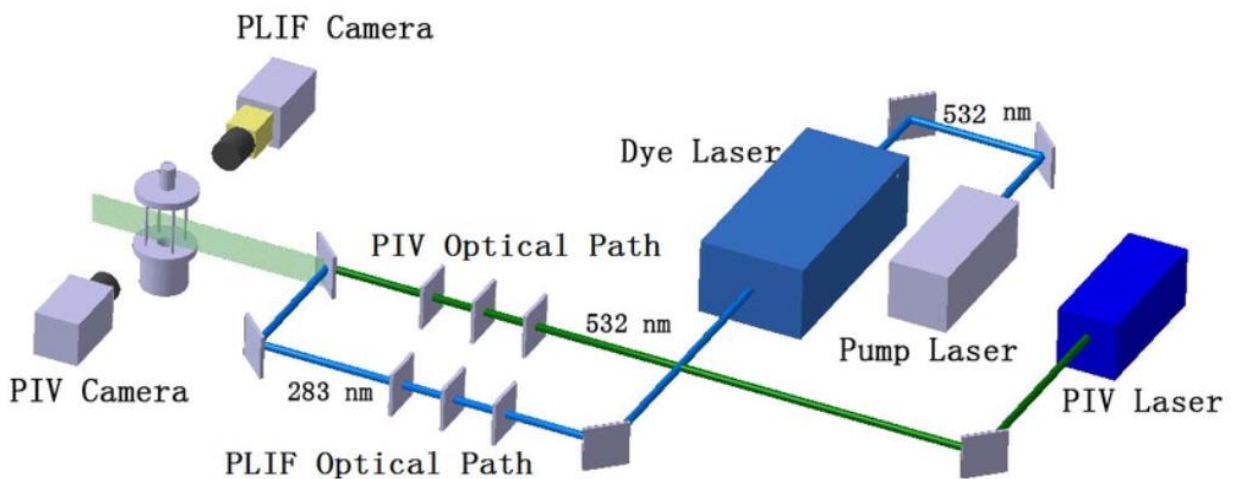
Figure 3. Operational diagram of a PLIF system using a 532 nm PIV laser sight source (An et al., 2016)

Limitations of the technology mainly come down to the requirement for a fluorescent

element to be added to the testing liquid during experiments, which can alter the properties of the

atomization. The technology is also sensitive to external fluorescent elements, such as

hydrocarbons, which can interfere and increase variance due to signal noise with the

measurement results.

The TDLAS system consists of a tunable diode laser light source, lenses arrangements,

and a signal detection system. Visible in the diagram in Figure 4, a diode laser is generated from

the system which directly transmits towards the active medium. Making use of the absorption

characteristics of certain mediums, the detector on the opposite end recognizes changes in the

emitted laser wavelength, which is recorded. (Wang et al., 2018) Using the Beer-Lambert Law,

the strength of the transmitted laser can be used to determine atomic concentrations in the

medium. Pressure, velocity, and temperature can also be extrapolated from this analysis process.
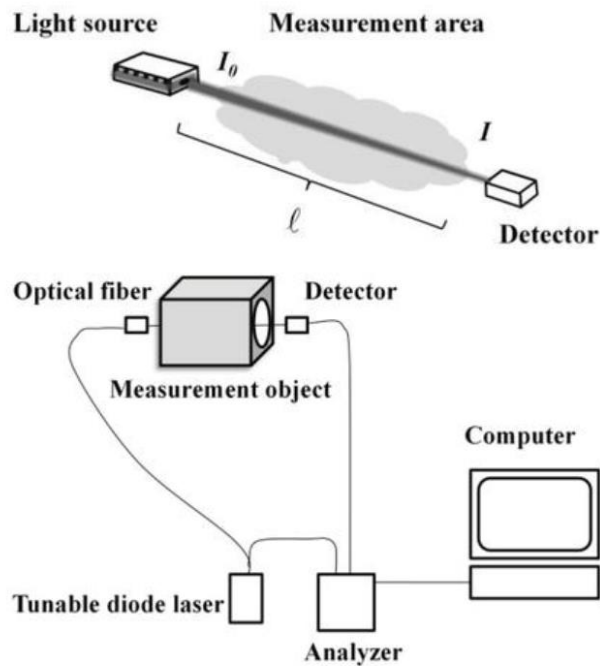
Figure 4. Operational diagram of a TDLAS system. (Wang et al., 2018)

Although TDLAS is limited in what mediums it can measure, it specializes in measuring

gas and liquid vapors who can absorb light, which align with the experimental elements of this

research. Like the PLIF system, it is also sensitive to external light sources, mainly due to the

technology's dependence on measuring small signal changes. Also, the technology uses a line-of-sight measurement technique, which only allows the measurement of a single dimension in-line with the detection laser. However, by integrating computed tomography to the system, a two-dimensional (2D) spatial distribution can be achieved, which is deem the tunable diode laser absorption tomography (TDLAT) system. Contrarily, implementation of this system will require at least the addition of a detectors array and laser pathing arrangements to be introduced into the experimental system.

3d. Optical imaging: high-speed photography

Another method of optical imaging is the use of high-speed photography. Using a capable photography device, the quick process of a liquid drop being launched and atomized can be recorded with intermittent frames that catch the drop and spray in still and clear motion, allowing accurate visual analysis of their properties.

Nowadays, high-speed photography is readily available in common consumer smartphones. Due to progression with images sensors which convert optical images into digital data, modern mobile smartphones have the capability to capture more frames per second (fps) beyond the 60fps standard frame rate of real time recording. Complementary Metal Oxide Semiconductor (CMOS) type image sensors are currently the newest and most popular imaging technology used in modern cameras devices. The result is that recorded video can be captured at a much higher framerate and replayed in 60 fps, essentially playing back the recording in slower motion than it was recorded. Modern mid-range to top-end phone will have the capability to achieve between 120 to 240 fps in 1920x1080 full high-definition resolution in the 1/8 speed slow motion recording setting. (GSM Arena, 2021)

However, in situations where an even higher amount of frame rate and high resolution are required to better capture still frames of motion, bespoke high-speed cameras can be used. Modern professional recording devices, like the Sony's Cybershot RX- 0 series (DSC-RX0 and DSC-RX0M2), have the capability to record 2 seconds worth of video in up to 960fps with 1920x1080 full high-definition resolution in high frame rate (HFR) mode. (Sony, 2018)

3e. Mechanical imaging: water sensitive paper

Besides imaging through optical photography, there are physical recording instruments that can capture resulting spray distribution and density. One of such tools that are used in the laboratory is water sensitive paper, developed by Syngenta back in 1985 for use with measuring agricultural low-volume ground spray distribution. By having a special yellow water-sensitive coating on top of each rigid paper sheet, the imprinting the water-based liquids can be recorded as the affected surfaces permanently changes to a blue color. Imprinting tolerance for the imaging medium is 0.002 mm. As a result, a two-dimensional distribution diagram can be collected with a high-resolution record of each droplet's final, post-drying circular area.

3f. Imaging Analysis Programs: ImageJ

ImageJ is a Java-based open-source software developed in 2007 by the Wayne Rasband and the Research Services Branch (RSB) in National Institute of Mental Health (NIMH), an umbrella of the National Institute of Health (NIH). This program can process, transform, and analyze user-defined distinctions in photos. (*Introduction - ImageJ*, n.d.) Image transformation can be performed within the program to increase droplet visibility using image thresholding and contrast adjustments. Utilizing the particle analysis function within ImageJ, the graphical size of

individual elements in a threshold-transformed photo can be recorded through pixel calculation and boundary algorithms. Results can then be parsed by the user and outputted on a datasheet file in comma-separated values (.csv) format. An example of this function is shown with a sample water sensitive paper image file below in Figure 5.
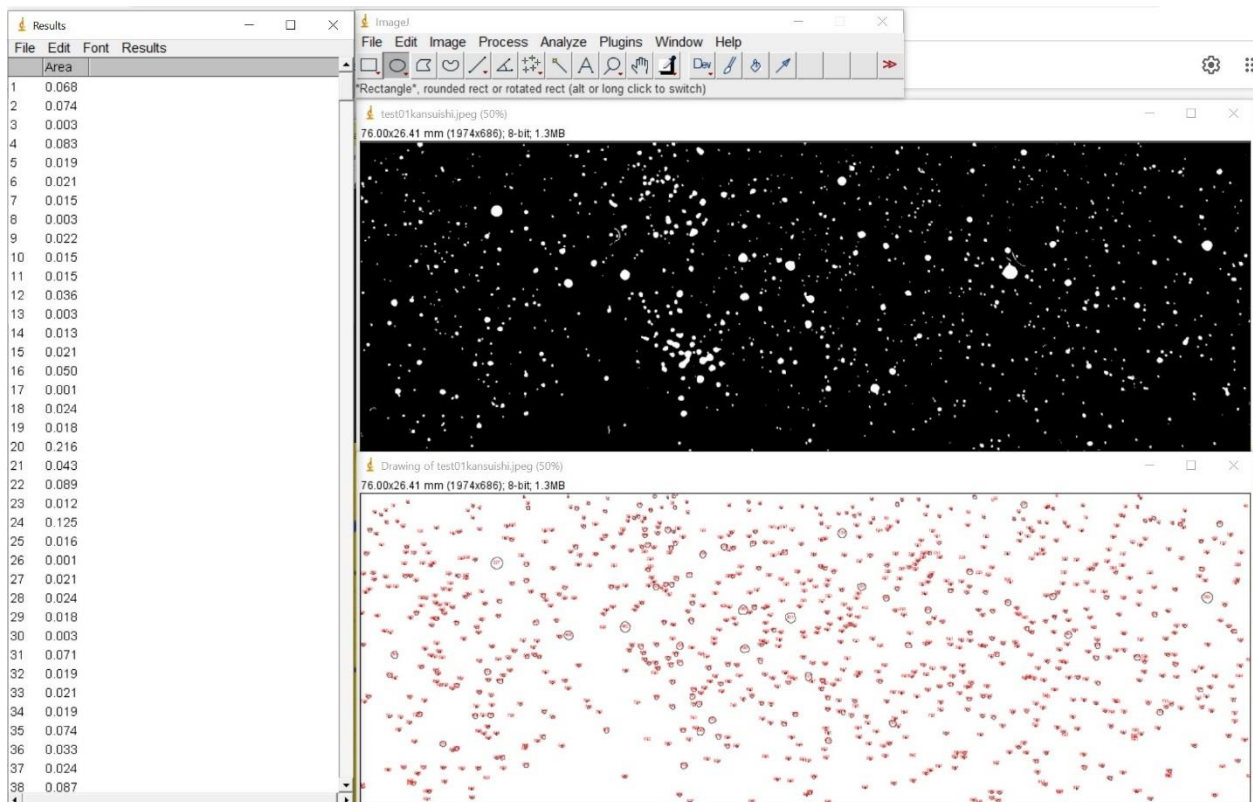
Figure 5. Calculating total quantity and individual area of circular spots on an image file with ImageJ

4. Current research of atomization in SIT

4a. Initial Research from Professor Hiroyasu Saito

The primary inefficiency in current combustion engines that Professor Saito's study sought to mitigate is the general heat loss that is applied to the ignited fuel spray that contacts the metal walls in a combustion chamber. This type of heat loss accounts for 20-30% of thermal efficiency in diesel engines. To begin studying the phenomenon of ultrasonic standing wave atomization in effort to control and reduce this heat loss, the experimental setup shown in Figure

6 below was created. The main oscillator/transducer, rated for use to mainly output and resonant around the 20kHz frequency, is the Langevin transducer HEC-3020P2B by Honda Electronics, mainly designed for use with ultrasonic-designed attachments in the manufacturing and processing industry. A matching diameter cylindrical reflector of 30 mm, milled of aluminum, was design to face directly across the transducer from 36 mm away. For generating the transducer's sine wave form, a power supply, NF wave generator, and voltage monitor were used. Testing liquid, which consists of a 50% by weight methanol and water aqueous solution, was outputted through a Hamilton Gastight syringe with a AS ONE syringe pump. Results of atomization were recording with the Photron Fastcam SA4 high-speed camera with a metal Halide Lamp illuminating the spray for increased optical visibility.
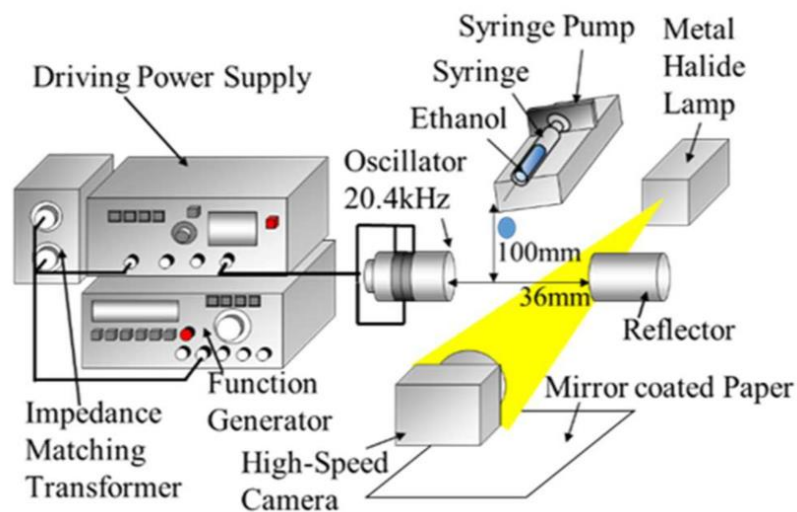
Figure 6. Experimental setup for atomization from Professor Saito's previous research

Tests were performed with the setup at around 20kHz, 160 Volts, at 0.3 Amps, generating a peak of around 48 Watts. The range of sound pressure to oscillator surface was analyzed by panning across the generated standing wave using a sound pressure measuring device. For this test, this select sound pressure measurement device and microphone setup was used: the RION UC-29 microphone, NH-05A preamplifier, and UN-14 sound level meter unit.

To analyze spray distribution, Professor Saito used ImageJ and has provided instructions, albeit in Japanese only, on the steps towards measuring liquid droplet area using the imaging processing program.

4b. Research breakthroughs and changes from master student, Tsubasa Nakamura

Currently, the experimental processes are followed from the previous master student who worked under Professor Saito, Tsubasa Nakamura. The behavior of atomization was further analyzed through data collection and synthesis and standing wave visualization.

To understand the accuracy of the experimental tools on hand, the imaging devices, a Koolertron 9-inch USB electronic microscope and Photron SA-4 high speed camera, were tested using a set size range of glass beads: GBL 40, 60, and 100. Results from the devices were proven acceptable for processing in ImageJ, where accuracy tolerance was measured to be 10-20 µm for beads sizes greater than GBL 60. The GBL 40, on the other hand, were visible in 1 to 5 pixels as recorded by the imaging devices but would result in highly inconsistent analysis within ImageJ, given the low resolution.
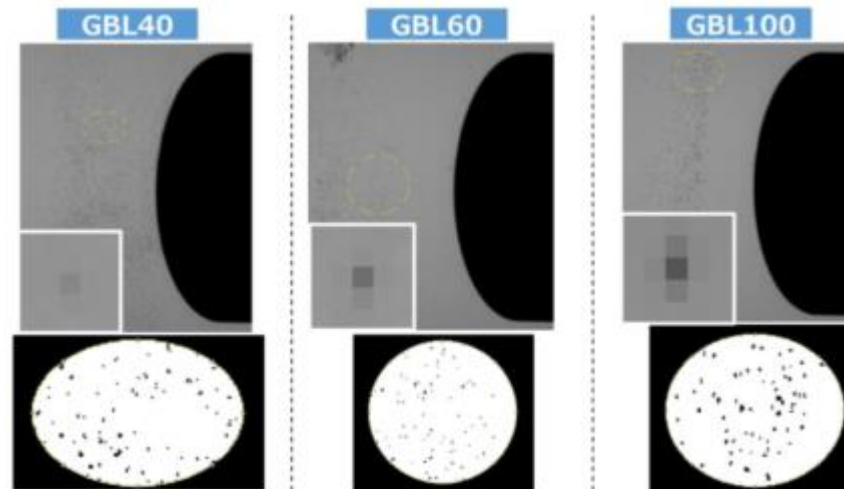
Figure 7. High speed camera still frame and electronic microscope scan of GBL beads

Droplet distribution behavior was observed and analyzed by using the electronic microscope on

the center of the translucent acrylic pane which had collected a small sample of the resulting

atomization. Initial atomization behavior was recorded pointing the Photron SA-4 camera

towards the node point, which was later used for analysis of droplet behavior in fragmentation.

For Nakamura's documented tests, a 50% by weight ethanol and water blend was used across the

following watt levels: 2.6-3.0W, 20W, 30W, 40W, and 50W.

The sound wave was visualized using the Rion UN14 sound level meter unit. The

external microphone was panned across the front of the transducer and reflector arrangement

while the transducer generated the following watt level: 2.6-3.0W, 20W, 30W, 40W, and 50W.

The data points were collected from the sound level meter at every millimeter and corrected from

the environmental background noise using the following equations (1.4.1, 1.4.2):

$$LC = -10 * \log10(1 - 10^{(-(LT - LB) / 10)}) \qquad (1.4.1)$$

$$SPL = LT - LC \qquad (1.4.2)$$

In these two equations, SPL is the adjusted target sound pressure value in decibel [dB], LT is the

recorded target sound pressure value in dB, LB is the background sound pressure value in dB,

and LC is the background noise correction value in decibels (dB). The adjusted sound pressure

value is then converted from decibel units to Pascal units using the following equation (1.4.3):

$$P_{sound} [Pa] = P_{air} * 10^{(SPL [dB]/20)} \qquad (1.4.3)$$

Figure 8 below shows the resulting generated sound pressure graph across the generated standing
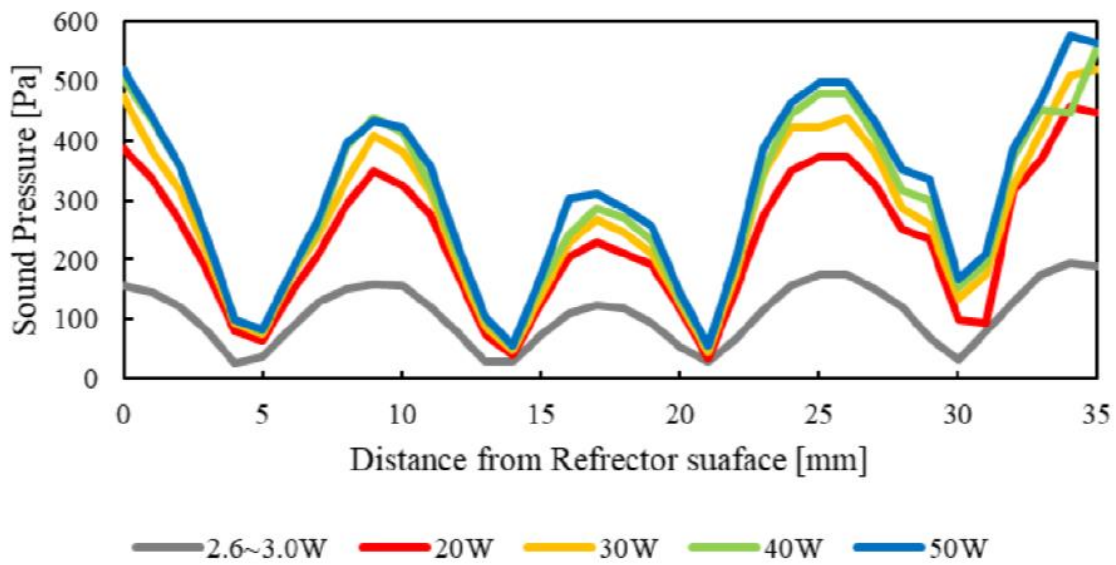
wave.

Figure 8. Measured sound pressure relative to distance from the reflector

Additional mechanical methods were used to visualize the standing wave as well. Light objects, like white tissue particles, were introduced and held in the standing wave nodes to determine the node locations during atomization trials. Trials with visualizing the standing wave with water vapors emitted underneath with a steam humidifier were attempted but failed.

Chapter 2: Methodology

Objective 1: Determine variable factors in water droplets atomization process

One of the most crucial factors to understand from experimentation with differing variables is the limits of which inhibit atomization. We were looking forward to finding the parameter limits in testing equipment, settings, and condition so that success and atomization consistency can be improved among finding relationships between variable factors and atomization performance.

Output power from the transducer was the main variable factor for us to study. The goal was to evaluate atomization at a variety of average watt levels to analyze the spray behavior using the experimental setup described earlier within section 4 of the background. Although we recorded the data for the frequency range and peak-to-peak voltage at which atomization occurs, we considered them resultant factors for the time being in the experiment since they were less controllable and will change due to environmental factors, such as laboratory temperature and humidity. In addition, since retaining power range for the transducer requires the constant modulation of frequency variable, atomization frequencies can be erratic and dependent on when resonance and atomization succeeds in the experiment.

Another aspect of the transducer that was recorded but treated as a resultant factor as well will be the distance between the transducer face and the reflector face. As described earlier with the equations (1.2.1) and (1.2.2), the distance is very much dependent on the length of the waveform which is affected by the current operational frequency. Since we were aware of the mathematical relationship between this distance and the standing wave characteristics, we solely collected data on this behavior to confirm this relationship.

The droplets were sent by gravity through a syringe. The production model and diameters of the syringe and syringe needles were recorded as they affect the droplet diameter. It is possible to assume that water tension, determined by the interfering surface area of the droplet to the needle tip, and the gravitational force upon the created droplet can differ based on needle inner and outer diameters. Currently, three varieties of syringe needles were at hand: the Hamilton 90022 (N722), 90026 (N726), 90030 (N730). The three needles were connected using a Luer Lock attachment hub to the Hamilton Gastight 1010LTT (81620) 10ml syringe and correlate to the following inner diameters: 0.41 mm, 0.26 mm, 0.15 mm. An optical recording of the water droplet leaving the needle were analyzed to determine the average droplet's initial shape based on each syringe type. Subsequent analysis of the water sensitive paper distribution will help analyze how water droplet size affects atomization performance.

The height of the droplet reaching the node of the standing wave can also be a variable factor. Previous experiments have left it at 100mm, but the current research would try to measure the difference between these elements. During testing, minimum height was set to 30mm since it will provide around 15mm worth of distance from the syringe with the transducers face, reducing the likeliness of the syringe disrupting the generated ultrasonic standing wave. Drag forces were assumed to impact the droplet's shape and velocity before it atomizes reaching the ultrasonic standing wave's node. However, due to time constraints of this research, the comparison of this variable has not been analyzed and testing resumed with the droplet height being set to 100mm.

The current mechanical collection tool for atomization spray results is water sensitive paper. Since water contacting the paper takes time to dry, these resulting spray droplet diameters can change from when the initial contact with the paper surface is made and when the paper is analyzed. Thus, results were calibrated by a synthesized calibration equation to improve the

accuracy of the resulting data. To find this calibration factor, a controlled test of collecting optical images of droplet sizes before and after drying was performed.

Objective 2: Collecting atomization distribution behavior of water droplets

To collect the whole distribution of spray from the experiment, a water sensitive paper array was affixed on top of a long wooden board, measuring 400x150 mm in area. A total of 10 sheets worth of 76x52 mm water sensitive paper sheets were attached to a grid paper, arranged and placed within our experimental setup as shown in Figure 9 and Figure 10 below. In the laboratory, 76x26 mm water sensitive paper sheets were also available for use if a differing water sensitive array layout was required. Board orientation, testing time, and other experimentation variables described in Objective 1 were recorded on the testing array for data organization.
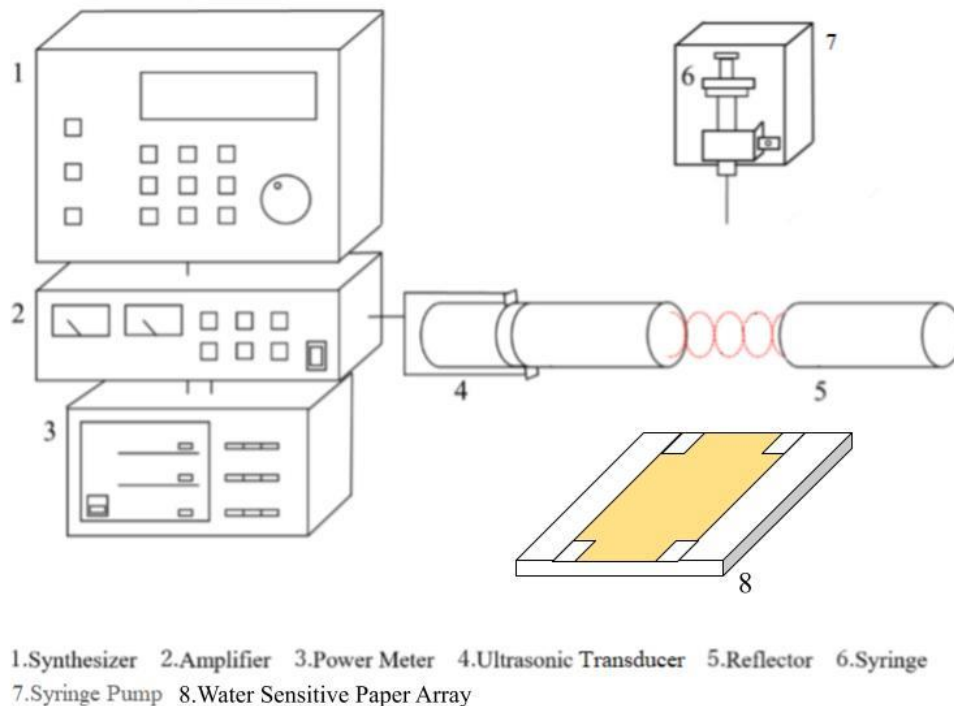

1.Synthesizer   2.Amplifier   3.Power Meter   4.Ultrasonic Transducer   5.Reflector   6.Syringe
7.Syringe Pump   8.Water Sensitive Paper Array

Figure 9. Current experimental setup for capturing droplet distribution on water sensitive paper
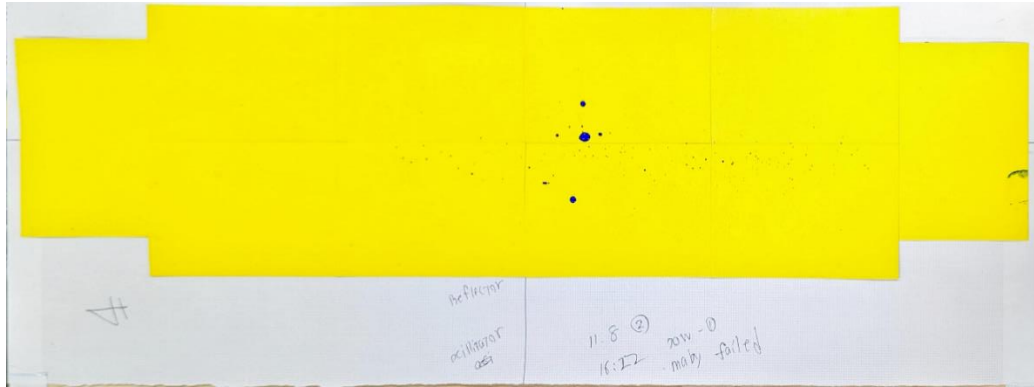
Figure 10. An example water sensitive paper sheet array affixed on a wooden board for collecting atomization results

The current experimental setup was designed for use with high-speed cameras for optical imaging. Past analysis of water droplet behaviors was performed with a Photron Fastcam SA4, which has the maximum frame rate of 3000 per second in 1024x1024 pixels. Sony Cybershot RX-0 still cameras were also in hand to perform the experiment which has a maximum frame rate of 960 fps at full high definition of 1920x1080 pixels. Handheld mobile smartphones were also capable for collecting high speed footage, granted with limits around 240fps maximum at full high definition for the Google Pixel 6 Pro and IPhone 13.

In the current laboratory, access to a YAG laser and delay generator among other optical recording devices, like the high-speed camera used in previous research, were given for use to construct a laser diagnostic-based experimental measurement setup if needed.

Objective 3: Post-processing atomization distribution images of water droplets

To analyze the distribution behavior, we will be testing digitizing our results on water sensitive paper with different tools and methods. In past experiments, resulting water sensitive paper sheets were only processed in the scanner at a maximum 600 dots-per-inch resolution. For data collection from the water sensitive paper during this research report, the Koolertron

electronic microscope will be used. The device possesses a 1000x digital and physical combined

magnification, allowing processing resolution to be user controlled with manual control of the

magnification lens and lighting as shown in operation collecting sample data in Figure 8 below.

Visual segmentation for analysis of a 76x52mm water sensitive paper sheet were evaluated to

determine the best compromise for optical resolution and efficiency of data collection and

processing.
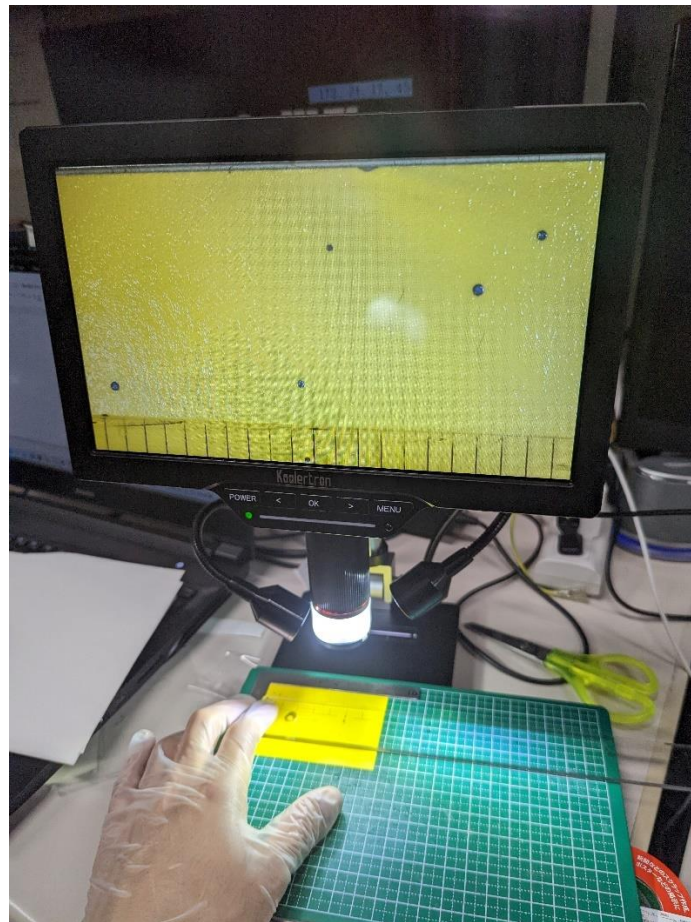
Figure 11. Koolertron 9-inch display and USB microscope device

Once test data was collected, we processed and analyzed the images within the ImageJ program.

Image files were saved through the microscope in Jpeg, which ImageJ was able to recognize and

use. As described earlier in section 3 of the background, the results of the analysis were parsed

by area and droplet count, outputted on a datasheet file in .csv format. The specific steps and

tools used in this process within ImageJ has been documented in a separate document file. Image files and datasheets were organized in an experimental data digital folder by test date, test time, and atomization power. From this data, the median diameter, mean diameter, and diameter histogram of each experiment were synthesized and compared. Additionally, visual observation of droplet distribution and atomization behaviors were recorded.

Each water sensitive paper sheet has their area and particle count data from each screenshot section combined. The simple diameter equation based on the area of the circle was used to find the average diameter of each droplet. Then, the compiled diameter values was used to find the D [3,2], or d_{32}, and D [4,3], or d_{43}, mean diameter of distribution for each droplet distribution section obtained with the following equations (2.3.1, 2.3.2):

$$D [3,2] = \sum D^3 / \sum D^2 \qquad\qquad\qquad (2.3.1)$$

$$D [4,3] = \sum D^4 / \sum D^3 \qquad\qquad\qquad (2.3.2)$$

D [4,3] was used to find the average diameter value for particular volumes distributions, also known as De Brouckere Mean Diameter, while D [3,2] was used to find the average diameter value for particular surface area distributions, also known as Sauter Mean Diameter (SMD). D [3,2] is most frequently used in specifications for fuel injection systems in the industry. D in these equations is the average diameter of each droplet.

Objective 4: Analyzing differences in behavior for other liquids in atomization mechanism

After being able to determine the relationships between current factors of the atomization experiment and the resulting atomization behavior of water droplets, we began integrating various types of liquid to determine the difference in behavior based on fluid characteristics. In

addition, we determined the feasibility of this experimental ultrasonic atomization setup in fragmenting and controlling atomization for differing combustion fuels. Within the laboratory, water and ethanol were available for use, so solutions with varying compositions of water and ethanol was created for testing.

Since water droplets were the main liquid element used in the current experiments, water sensitive paper sheets were properly relied on to record spray variables. However, for non-aqueous solutions that might be tested in this setup, a new mechanical or optical imaging tool will be required for installation on the experimental setup.

Chapter 3: Results

1. Initial droplet diameter relative to diameter on water sensitive paper
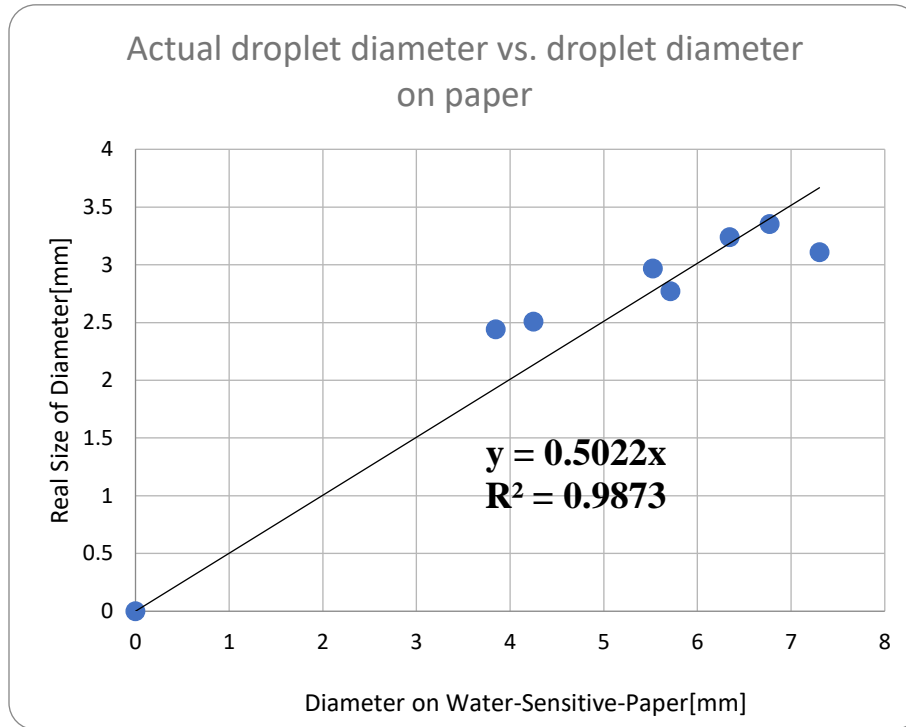
Figure 12. Calibration graph between observed droplet diameter and recorded droplet diameter on water sensitive paper with linear line of best fit

The graph shown in Figure 12 was created to allow the proper analysis of collected liquid droplets on the water sensitive paper, which expand as they initially compress and dry on the paper surface. The initial observed droplet diameter was taken from two controlled droplet tests from each of the three available needle sizes. Alternatively, a synthesized equation (3.1.1) from a previous research using ImageJ and water sensitive paper for spray analysis can also be used, which is the following: (Zhu et al., 2011)

$$D = 1.06 \, A^{0.455} \tag{3.1.1}$$

In this equation, A represents the droplet area as analyzed on the water sensitive paper surface with ImageJ and D represents the adjusted real diameter of the droplet. In the following results

section, frequency distributions and mean diameter comparisons will be using the former synthesized function. Due to time restraints, this calibration test cannot be performed for the water/ethanol blends that were used in the experiment, which may imprint differently on the water sensitive paper surface due to quicker evaporation.

2. Comparison of pure water droplet atomization between 70W and 60W
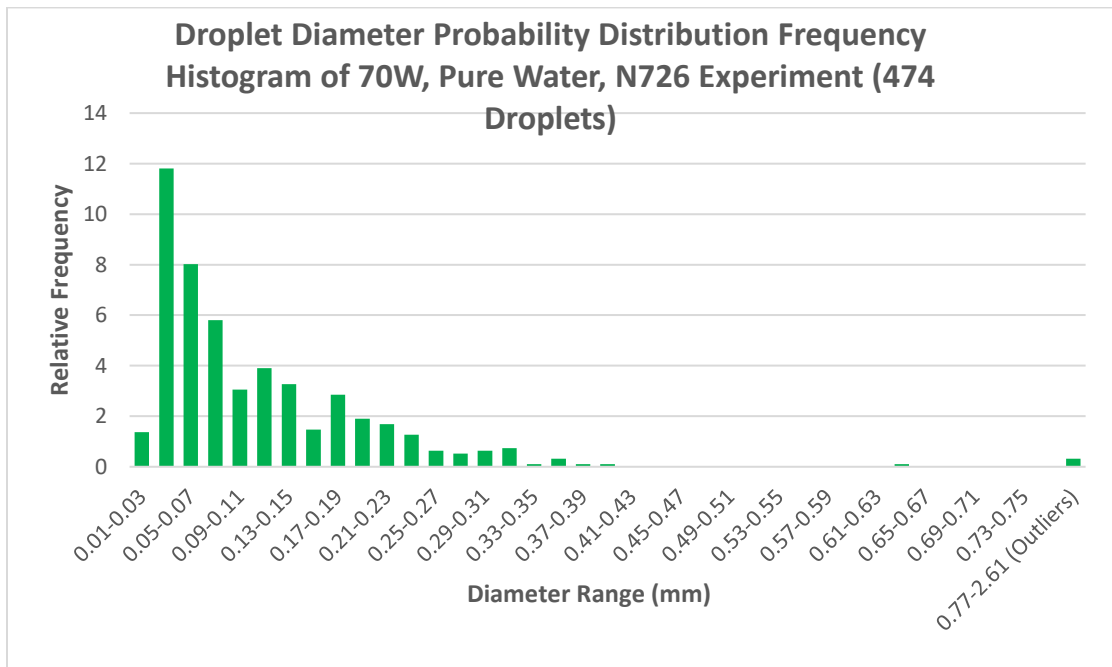
Figure 13. Droplet Diameter Probability Distribution Frequency Histogram of 70W, Pure Water, N726 Experiment

Figure 14. Droplet Diameter Probability Distribution Frequency Histogram of Left side of 60W, Pure Water, N726 Experiment

This comparison was chosen to determine, among pure water, what the effect of differing standing wave power level would alter in the overall droplet distribution and mean diameter during atomization. The D [3,2] and D [4,3] for the 70W test in Figure 13 was 0.658 mm and 1.148 mm. D [3,2] and D [4,3] for the 60W test in Figure 14 was 0.439 mm and 0.950 mm, with a difference of around 0.121mm and 0.198 mm. If large diameters exceeding 1mm were removed from the data pool, justified by being incompletely atomized sections of the water droplet, the D [3,2] and D [4,3] for the 70W test is around 0.214 mm and 0.251 mm and for the 60W test is around 0.176 mm and 0.229 mm, with a difference of around 0.038 mm and 0.022 mm.

3. Comparison of 50%wt ethanol/water droplet atomization between 50W and 40W

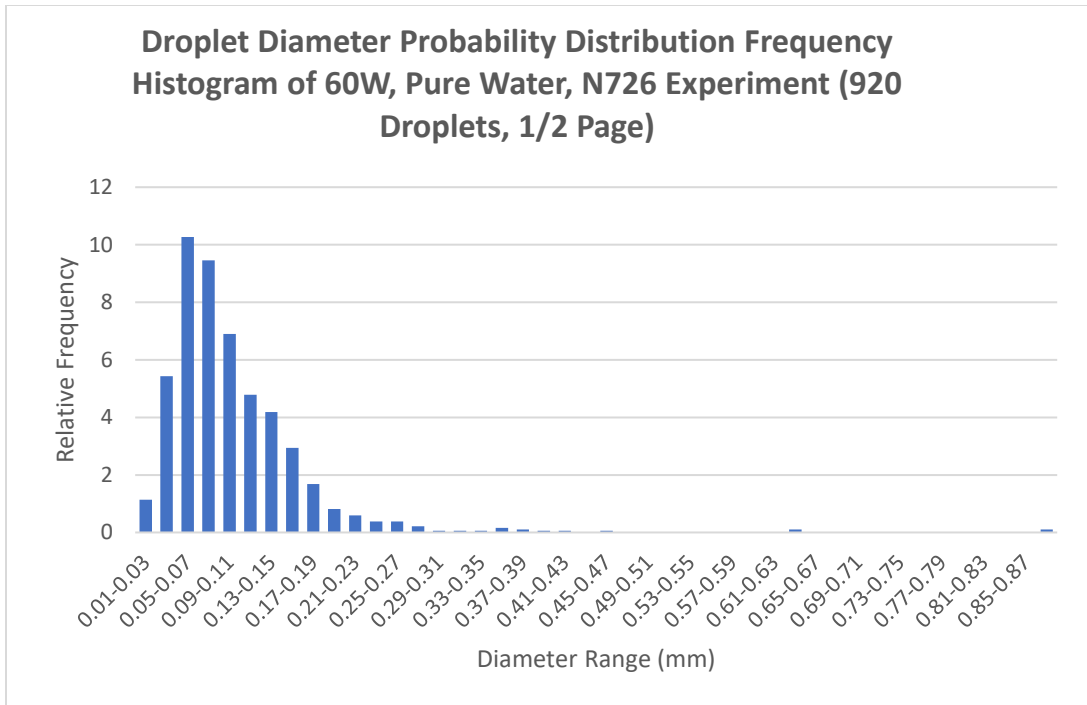*Figure 15. Droplet Diameter Probability Distribution Frequency Histogram of 50W, 50%wt Ethanol/Water Solution, N726 Experiment*

Figure 16. Droplet Diameter Probability Distribution Frequency Histogram of 40W, 50%wt Ethanol/Water Solution, N726 Experiment

The previous comparison objective was repeated for a 50%wt ethanol/water solution to observe

if the characteristics from the previous comparison will differ using a different liquid type. The D

[3,2] and D [4,3] for the 50W test in Figure 15 was 0.332 mm and 0.759 mm. D [3,2] and D [4,3]

for the 40W test in Figure 16 was 0.450 mm and 1.170 mm, with a difference between 0.118 mm

and 0.411 mm. With large diameter droplets exceeding 1mm removed from the data pool, D

[3,2] and D [4,3] for the 50W test is around 0.234 mm and 0.414 mm and for the 40W test is

around 0.202 mm and 0.375 mm, with a difference between 0.022 mm and 0.039 mm.

4. Comparison of 60W atomization between pure water and 50%wt ethanol/water

   solution

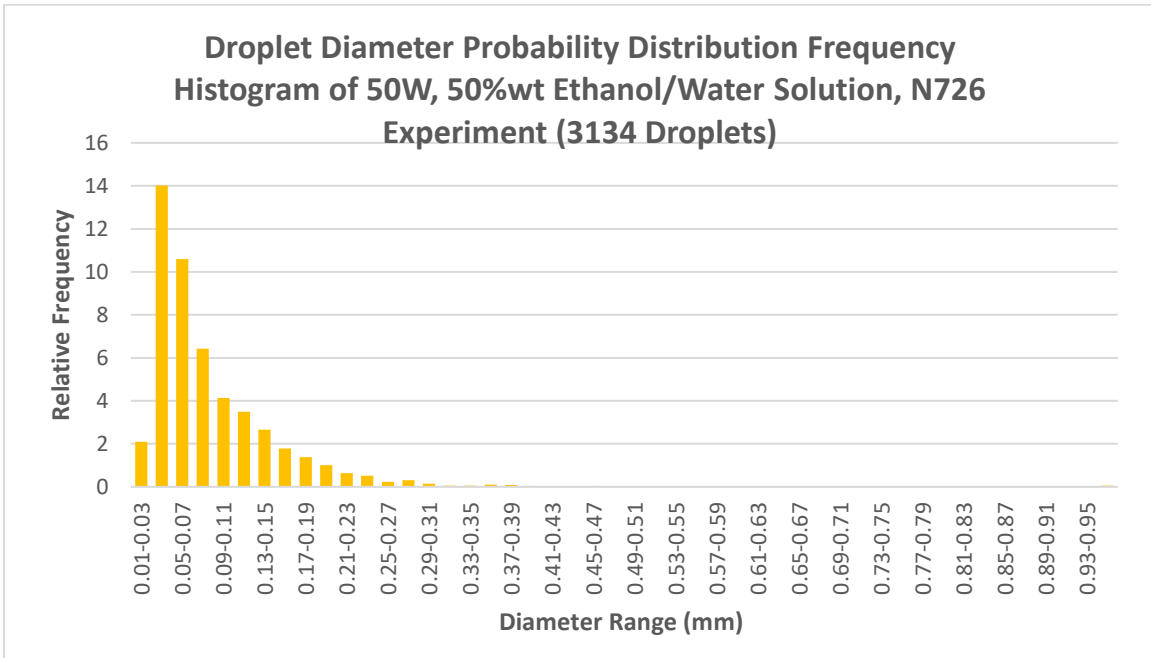*Figure 17. (Repeated) Droplet Diameter Probability Distribution Frequency Histogram of 60W, Pure Water, N726 Experiment*
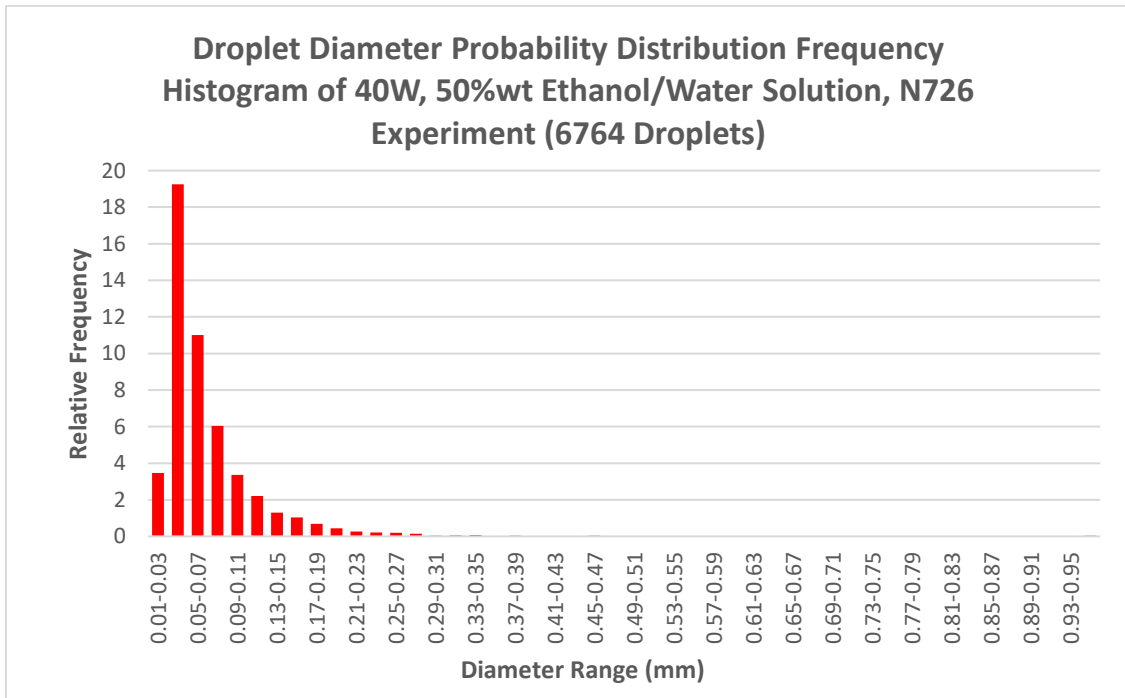
Figure 18. Droplet Diameter Probability Distribution Frequency Histogram of 60W, 50%wt Ethanol/Water Solution, N726 Experiment

The following comparison details the performance of the atomization process relative to different liquid types, which share differing density, surface tension, and viscosity. The D [3,2] and D [4,3] for the pure water test in Figure 17 was 0.439 mm and 0.950 mm. D [3,2] and D [4,3] for the 50%wt ethanol/water blend test in Figure 18 was 0.223 mm and 0.391 mm, being notably lower than the pure water test by 0.216 mm and 0.559 mm. With large diameter droplets exceeding 1mm removed from the data pool, the D [3,2] and D [4,3] for the pure water test is around 0.176 mm and 0.229 mm, which, accepting the adjusted results viable for comparison, would assume nearly similar performance among the two tests, with a difference of 0.047 mm and 0.162 mm. Interestingly, the 50%wt ethanol/water blend didn't produce droplets over the size of 1mm. Its outliers were around the 0.69-0.71mm range.

5. Comparison of water atomization at 70W between N726 needle and N722 needle
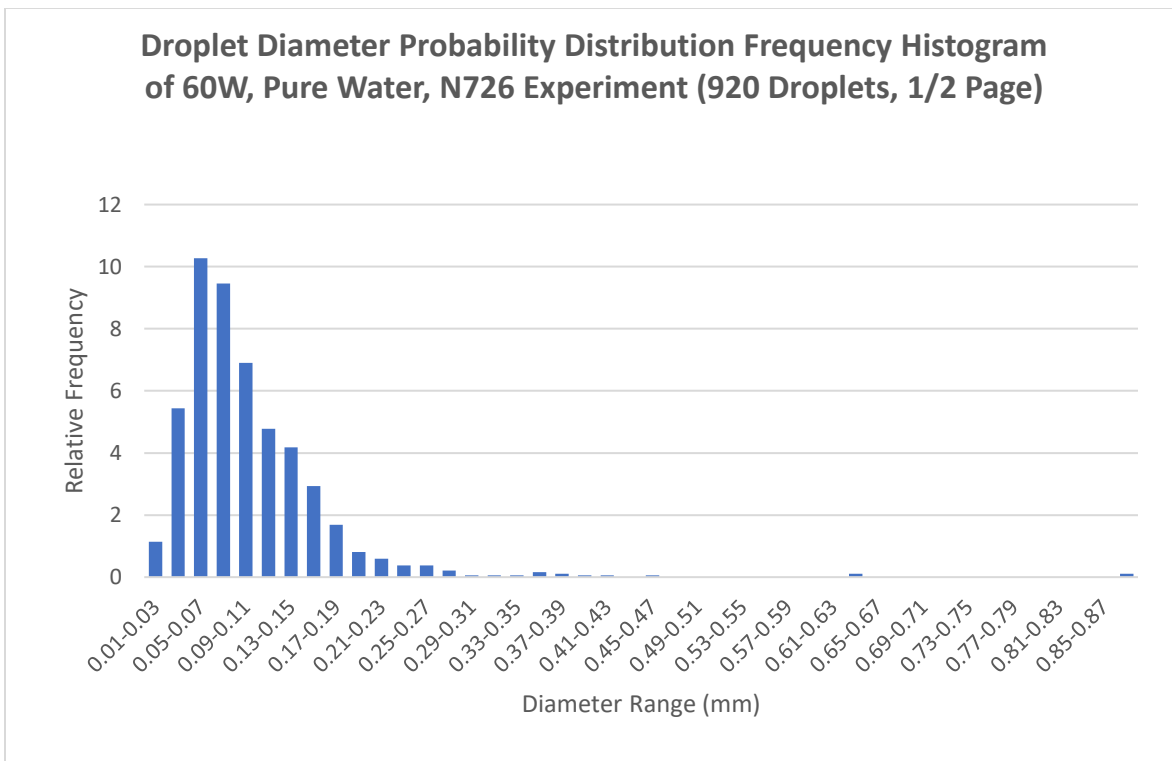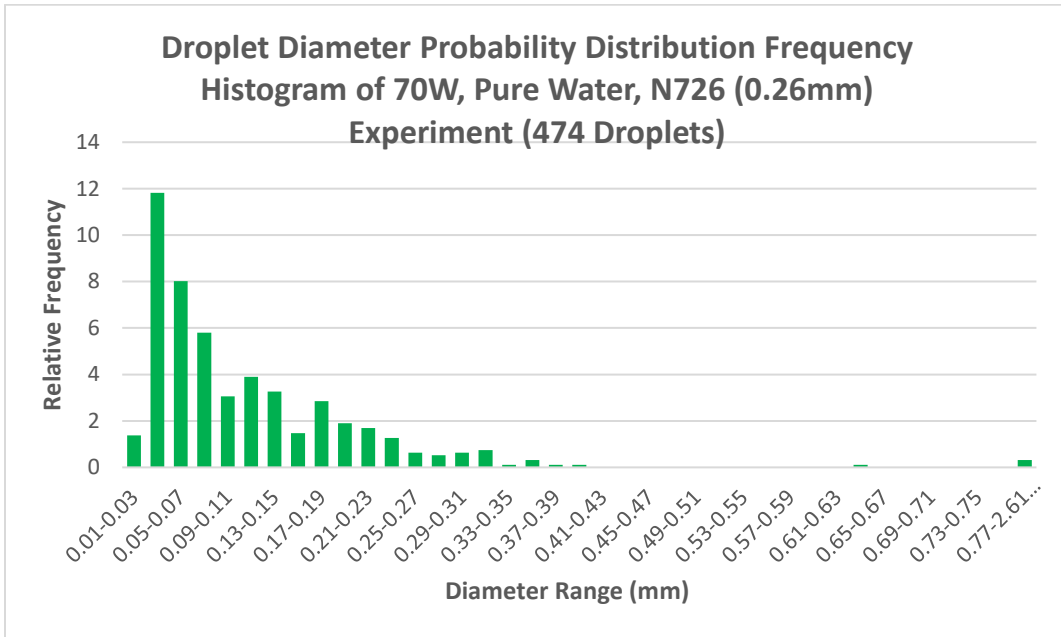

Figure 19. (Repeated). Droplet Diameter Probability Distribution Frequency Histogram of 70W, Pure Water, N726 (0.26mm) Experiment

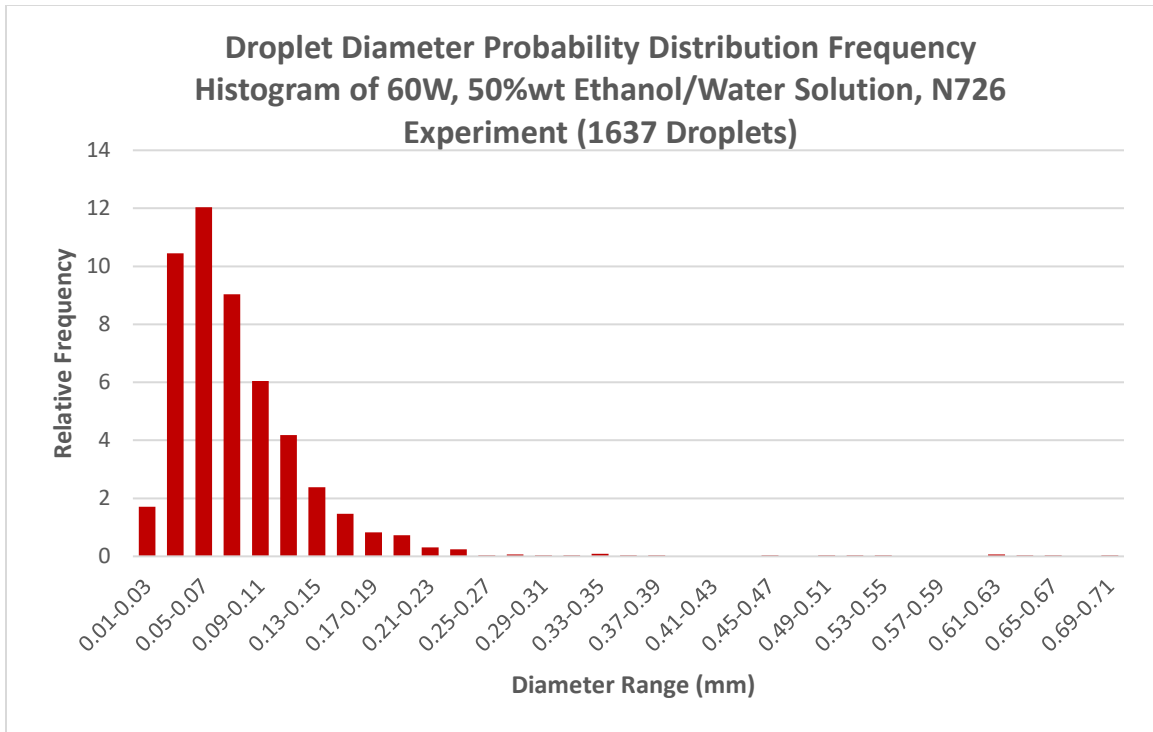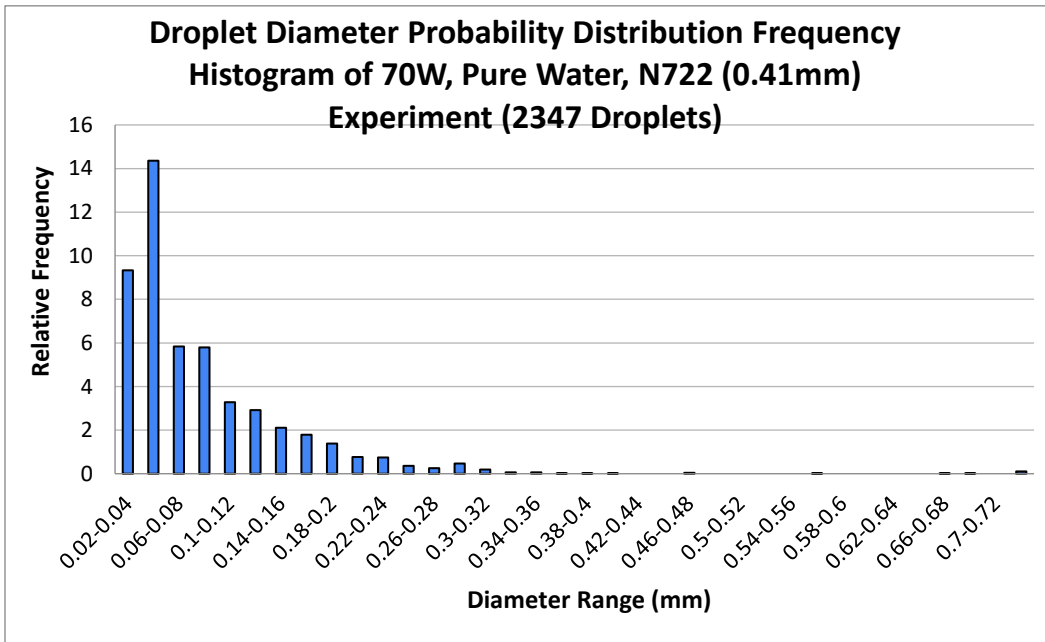Figure 20. Droplet Diameter Probability Distribution Frequency Histogram of 70W, Pure Water, N722 (0.41mm) Experiment

The following comparison was made to determine contrasts in performance of our experimental setup based on changing droplet sizes, generated from differently sized inner diameter outlet point, which in the case of this experiment are syringe needles. The D [3,2] and D [4,3] for the N726 test in Figure 19 was 0.658 mm and 1.148 mm. D [3,2] and D [4,3] for the 40W test in Figure 16 was 0.487 mm and 1.070 mm, a total difference of around 0.171 mm and 0.078 mm. With large diameter droplets exceeding 1mm removed from the data pool, D [3,2] and D [4,3] for the 50W test is around 0.234 mm and 0.414 mm and for the 40W test is around 0.202 mm and 0.375 mm, with a difference around 0.032 mm and 0.039 mm.

6. Reevaluation of the standing wave shape using a sound pressure measuring device

Figure 21. Remeasured sound pressure relative to distance from the reflector

To compare the experimental conditions of the current sanding wave to previous experiments, the standing wave shape was reevaluated using a Rion UJ14 sound level meter. An

additional recording of the standing wave at 60W was performed to provide visual data on the experimental setting that closer aligns with the increased power input during testing that current research has been progressing into.

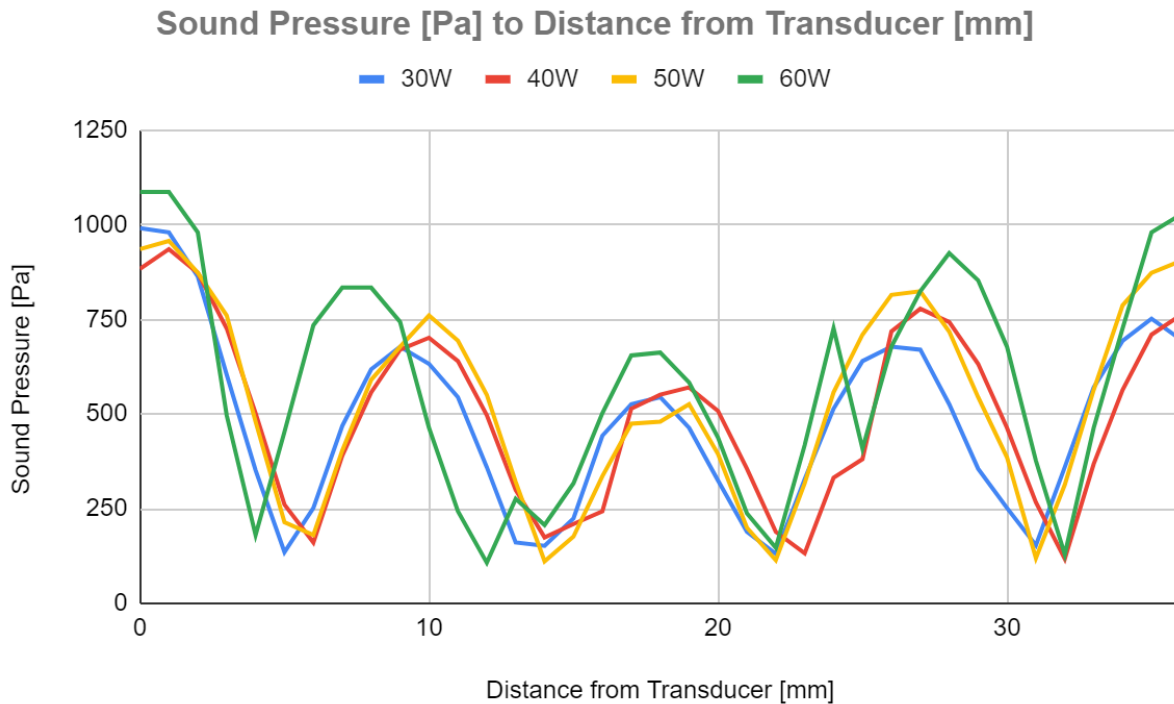The resulting visual graph shows a similar generated waveform as the previous experiments, generating 4 nearly equidistant nodes and an amplitude that reduces when reaching the center of the distance between the transducer and reflector. At each node, regardless of standing wave power level, the waveform nearly reaches the same minimum sound pressure level. However, sound pressure level ranges between the two experiments are different, with the current waveform having a sound pressure range from around 200-1100 Pa while the past waveform, shown in Figure 8, shows the setup generating a sound pressure range between around 50-540 Pa. Exclusively in the current waveform evaluation, the 60W waveform shows a larger maximum generated sound pressure increment from a waveform 10-watt power lower than seen with the rest of the waveforms in both evaluations. Increments near the point of the antinode nearly increased from the 50W waveform at about 125 Pa.

7. Observation of water droplet from slow motion recording

In the recent course of research, an additional recording of the atomization process at 60W with a N726 needle has been made using the smartphone camera, recording at 1/8 speed, 240 frames per second, as a point of comparison with the high-speed video taken from the previous research. Screenshots from both recordings can be seen in below in Figure 22 and Figure 23.
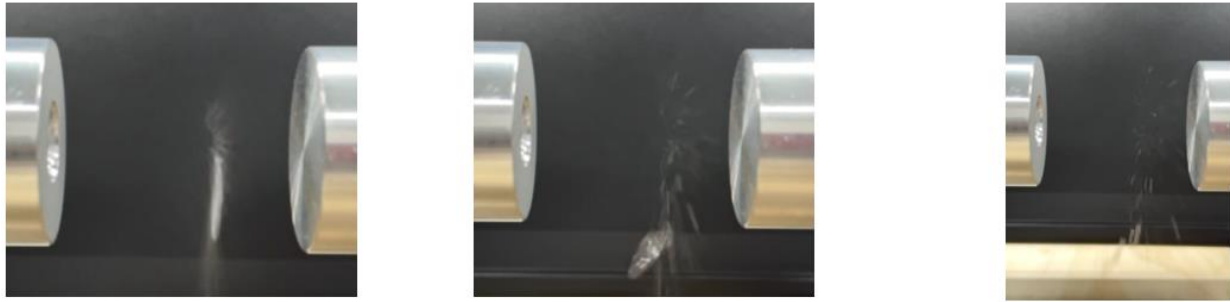
Figure 22. Screenshots from slow motion smartphone recording of pure water atomization at 60W
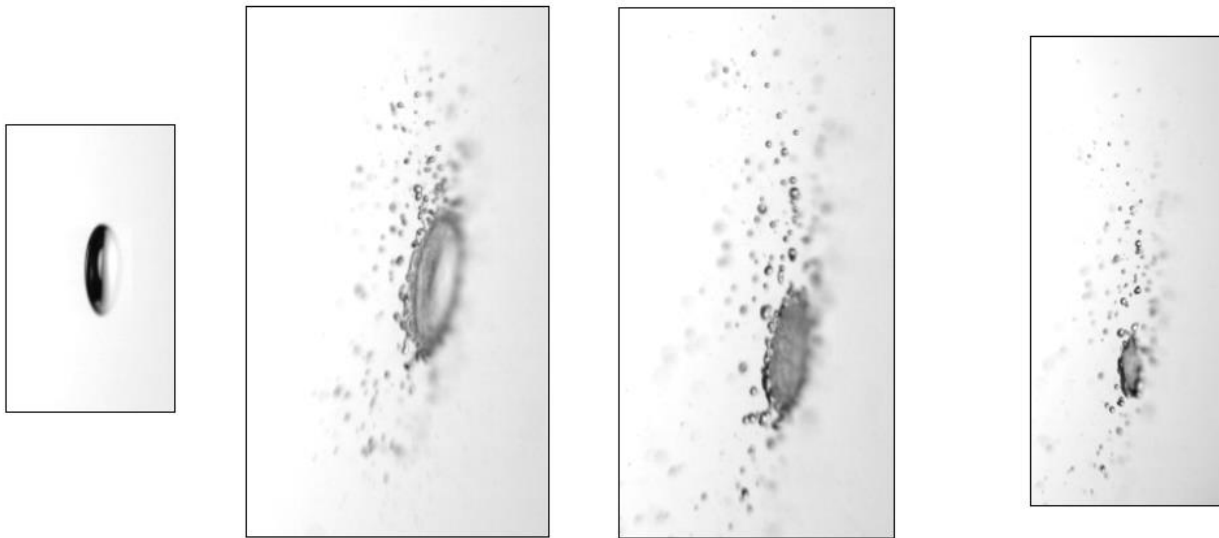
Figure 23. Screenshots from the slow motion camera recording of pure water atomization with the Photron SA-4

8. Comparison of Median Diameter from experiment data

To figure out the behavior of the atomization effects generated by our experimental setup aligns with existing atomization principals, we can calculate the median diameter of our result data from before and compare their results to those obtained by equation (1.3.1) synthesized from Lang. (Lang, 1962). Surface tension for the 50%wt ethanol/water solution and pure water was obtained using a published surface tension table for alcohol and water between 20 to 50 degrees Celsius (Vazquez et al., 1995). Density value was collected from an online table of density relative to ethanol and water blend by mass (Engineering Toolbox, n.d.).

Test	Median Diameter (Data) (mm)	Median Diameter (Calculated) (mm)	Frequency (hz)	Surface Tension (mN/m)	Density (g/L)
70W, Water, N726	0.08308481	0.056828458	19806	72.75	0.998202
70W, Water, N722	0.064610551	0.056832284	19804	72.75	0.998202
60W, Water, N726	0.087788451	0.056801312	19820.2	72.75	0.998202
60W, 50%wt Ethanol, N726	0.07167897	0.042769488	19829.7	28.51	0.91546
50W, 50%wt Ethanol, N726	0.067049537	0.042776248	19825	28.51	0.91546
40W, 50%wt Ethanol, N726	0.053759228	0.042744631	19847	28.51	0.91546

Table 1. Calculated comparison between recorded median diameter in comparison with median diameter calculated used Lang's equation: $D = 0.34(8\pi T/\rho F^2)^{1/3}$

As visible from Table 1, the resulting calculated median diameter is unfortunately quite different from the collected median diameter. It is possible that differences in the experimental environment and setup used to perform the atomization might be introducing unknown factors into the resulting droplet diameters.

Chapter 4: Discussion

1. Behavior and comparison among liquid droplet tests

The 60W pure water and 50%wt ethanol/water test, seen in Figure 14, Figure 17, and Figure 18, share unique comparison characteristics from the other test results. First, the distribution histograms for the two tests share a uniquely softer J-shape, nearing a bell curve shape for its overall distributional histogram compared to other tests result example. Most test examples carry a sharper J-shape curve, with the greatest sample diameter frequency range having a greater frequency difference than the neighboring range, The 60W tests also share a later peak than other test data, being around the 0.05-0.07 mm range when most test data hold the frequency peak at around 0.03-0.06 mm.

An unexpected behavior that the tests seem to share is the inverse correlation between standing wave power output and generated droplets. It may be assumed that the greater pressure at the node from the stronger standing wave will correlate to greater atomization density and reduced generated droplet diameter and therefore, with the same volume of liquid in each comparison test, a greater number of droplets will be produced. However, droplet amounts will double as the standing wave power levels reduce at 10-watt intervals, as shown between the N726 50%wt ethanol/water solution test at 50W, 40W, and 60W, seen in Figure 15, Figure 16, and Figure 18, respectively. Theoretically, between the N726 needle tests for water at 70W and 60W (seen in Figure 13 and Figure 14) that droplet difference can nearly be quadrupled with pure water, which cannot be solidly proposed due to the limited data for the 60W pure water test. In addition, the comparison between the two liquid types at 60W show that atomized droplet amounts tend to be similar among different liquid types.

It could be possible that there was a greater density of droplets, but the droplets were too small and generated a surface area impression too light to be picked up by ImageJ. Another assumption can be made that the distributed droplets might have overlapped other droplets and imprinted above existing droplets on the water sensitive paper. Outliers between the tests seem to be relatively similar in terms of size and distribution, so the possibility of the result being due to less of the droplet being atomized can be ruled out.

Although the atomization performance comparison made between the two 60W tests show the differing liquids atomizing behavior being nearly the same, the other collected data of atomized 50%wt ethanol/water solution shows the best overall diameter range frequency, with the 40W test in Figure 16 holding the steepest J-curve out of all the synthesized experiments. Additional tests to see if pure water can produce similar behavior can be helpful in determining whether the standing wave power and individual liquid properties are independently or collaboratively causing this behavior, but pure water has a lower limit of atomizing only above 60W during testing.

2. Droplet initial fragmentation observation

Both water droplet recordings, though the recent recording in Figure 22 is more limited for use in analysis due to the reduced frame rate, show similar atomization process. More closely visible in Figure 23, we can see that exactly when reaching the node, the droplet quickly shears vertically and bursts out atomized fine smaller droplets. An outer lining surface can be seen that folds out and away towards the right of the fine droplet burst, much like a liquid filled balloon being popped. This lining is then seen reforming into a large droplet and, due to weight and acceleration due to gravity, quickly falls ahead of the droplet distribution. It seems that this characteristic behavior of the atomization is causing the large droplet outliers, where the outer

droplet layer cannot fragment due to the crushing atomization method used in this experimental setup.

The observation also visually aligns with the description of ultrasonic atomization due to the introduction of inner droplet capillary waves in Lang's research, causing the outer droplet surface lining to burst once the waves exert a greater force than the surface tension holding the droplet together (Lang, 1962). Unfortunately, it seems that the experimental procedure is too different for Lang's synthesized equation (1.3.1) for the resulting diameter values to demonstrate any correlation, a seen in the results section. Alternatively, the crushing force at the node of the water droplet can also be a supporting or main factor of atomization that causes the droplet to split near center and burst. This or another mechanism would lead to a different mean diameter from Table 1.

3. Evaluated standing wave shape observations

With the sizable difference in sound pressure generation ranges, as seen in the resulting graphs of the waveform in Figure 8 and Figure 21, the alteration can be assumed to have been caused by the replacement with a new transducer, albeit with the same make and model, that occurred in the beginning of this research period when the previous transducer had failed. The previous transducer had been used in Professor Saito's laboratory, up until it had failed at the beginning of this research period, for around 4 years. Additional notable differences include the overall less uniform wave output of the current waveform, with the previous waveform showing standing waves at differing power level sharing equally shaped waves with a minor displacement in sound pressure amplitude. Differences among antinode amplitudes are also better defined in the previous waveform evaluation, with each increment of 10-watt power showing a slight increment to the maximum generated sound pressure.

Chapter 5: Conclusion

Observing the general diameter frequency and distribution and SMD for the compiled tests in the section before, the data overall proved an unexpected behavior in the atomization process: the standing wave watt power level had an inverse relationship with the total atomized droplet amount, nearly doubling the number of droplets atomized per 10-watt level decrease. In most case for all the experiments performed, droplet distribution tended to share similar J-shape form and have a frequency peak around 0.03-0.06 mm. Droplet diameter due to standing wave power level, in terms of D[3,2] and D[4,3], was shown to have a notable decrease between around 0.120 to 0.400 mm including outlier large diameter droplets over 1mm and about 0.02 and 0.04 mm with the outliers removed from the data sample. With the change of the inner needle diameter that output the droplet from 0.026 mm to the larger 0.041 mm needle, the mean diameter decreased by a small yet noticeable amount: D[3,2] of 0.171 mm and D[4,3] of 0.078 mm accounting large droplets and 0.032 mm and 0.039 mm without large diameters. However, due to the small sample group that was used for these comparisons, the overarching effects of these factors cannot be properly quantified yet or conclusive.

1. Recommendations:

Currently, we have a variety of tests with differing surface tension levels and power levels which haven't been analyzed into diameter distributions yet. With complete compilation of that data, we can develop an average diameter curve to supply data that can better show the behavior relative to each element. Additional accuracy can also be had by reproducing the experimental tasks shown in the results section to reduce outliers and stabilize the resulting correlation behavior. Additional experimentation and observation tasks around the ultrasonic experimentation setup should be devised to improve our understanding of how the ultrasonic

standing wave disrupts and atomizes the falling droplet. One such experimentation is the atomization performance relative to the distance of the droplet falling towards the standing wave node, which can determine the effects of drag forces and droplet velocity and acceleration relative to atomization performance. Once the additional data is compiled from the completion of these recommended experimentation task, the new variety of knowledge extrapolated can help alter the current experimental setup's atomization process to mitigate large diameter atomized droplets and improve the performance of the experimental standing wave atomization method.

Bibliography

An, Q., Kwong, W. Y., Geraedts, B., & Steinberg, A. (2016). Coupled dynamics of lift-off and

    precessing vortex core formation in swirl flames. *Combustion and Flame*.

    https://doi.org/10.1016/j.combustflame.2016.03.011

Dahham, R. Y., Wei, H., Pan, J., & Link to external site, this link will open in a new window.

    (2022). Improving Thermal Efficiency of Internal Combustion Engines: Recent Progress

    and Remaining Challenges. *Energies*, *15*(17), 6222. https://doi.org/10.3390/en15176222

Engineering Toolbox. (n.d.). *Ethanol Water Mixtures—Densities vs. Temperature*. Retrieved

    December 1, 2022, from https://www.engineeringtoolbox.com/ethanol-water-mixture-

    density-d_2162.html

GSM Arena. (2021). *Google Pixel 6 Pro—Full phone specifications*.

    https://www.gsmarena.com/google_pixel_6_pro-10918.php

Haga, N. (2011). *Combustion engine power plants*. 16.

Introduction—ImageJ. (n.d.). Retrieved November 8, 2022, from

    https://imagej.nih.gov/ij/docs/intro.html

Lang, R. J. (1962). Ultrasonic Atomization of Liquids. *The Journal of the Acoustical Society of*

    America, *34*(1), 6. https://doi.org/10.1121/1.1909020

Lefebvre, A. H., & McDonell, V. G. (2017). *Atomization and Sprays (2nd Edition)* (2nd ed.).

    CRC Press. https://app-knovel-com.ezpv7-web-p-

    u01.wpi.edu/web/view/khtml/show.v/rcid:kpASE00028/cid:kt011MGYH1/viewerType:k

    html//root_slug:atomization-sprays-2nd/url_slug:general-

    considerations?cid=kt011MGYF7&b-toc-cid=kpASE00028&b-toc-root-

    slug=atomization-sprays-2nd&b-toc-

title=Atomization%20and%20Sprays%20%282nd%20Edition%29&b-toc-url-slug=general-considerations&kpromoter=federation&page=1&view=collapsed&zoom=1

Luo, X., Cao, J., He, L., Wang, H., Yan, H., & Qin, Y. (2017). An experimental study on the coalescence process of binary droplets in oil under ultrasonic standing waves. *Ultrasonics Sonochemistry*, *34*, 839–846. https://doi.org/10.1016/j.ultsonch.2016.07.024

Shields, L. (2021). Greenhouse Gas Emissions Reduction Targets and Market-based Policies. *National Conference of State Legislatures (NCSL)*. https://www.ncsl.org/research/energy/greenhouse-gas-emissions-reduction-targets-and-market-based-policies.aspx#:~:text=The%20new%20law%20establishes%20GHG,zero%20GHG%20emissions%20by%202050.

Sony. (2018). *Sony RX0 II 1" (1.0-type) sensor ultra-compact camera | DSC-RX0M2*. Sony Electronics. https://electronics.sony.com/imaging/compact-cameras/all-compact-cameras/p/dscrx0m2-b

Toyota, K., Hirota, M., & Saito, H. (2019). Influence of ultrasonic standing wave on the atomization characterisitc of falling droplets. 微粒化シンポジウム, *28*.

University of Tennessee. (n.d.). *Standing waves*. Retrieved November 10, 2022, from http://labman.phys.utk.edu/phys221core/modules/m11/Standing_waves.html

U.S. Energy Information Administration (EIA). (2019). *Natural gas-fired reciprocating engines are being deployed more to balance renewables*. https://www.eia.gov/todayinenergy/detail.php?id=37972

U.S. Energy Information Administration (EIA). (2022, October 12). *Short-Term Energy Outlook*. https://www.eia.gov/outlooks/steo/report/global_oil.php

Vazquez, G., Alvarez, E., & Navaza, J. M. (1995). Surface Tension of Alcohol Water + Water from 20 to 50 .degree.C. *Journal of Chemical & Engineering Data*, *40*(3), 611–614. https://doi.org/10.1021/je00019a016

Wang, Z., Kamimoto, T., Deguchi, Y., Wang, Z., Kamimoto, T., & Deguchi, Y. (2018). Industrial Applications of Tunable Diode Laser Absorption Spectroscopy. In *Temperature Sensing*. IntechOpen. https://doi.org/10.5772/intechopen.77027

Xing, F., Huang, Y., Zhao, M., & Zhao, J. (2016, February 14). *The Brief Introduction of Different Laser Diagnostics Methods Used in Aeroengine Combustion Research*. https://www.hindawi.com/journals/js/2016/2183569/

Yang, Z., Tao, R., Chen, L.-A., Zhong, K., & Chen, B. (2020). Feasibility study on improving the performance of atomization liquid desiccant dehumidifier with standing-wave ultrasound. *Energy*, *205*, 118101. https://doi.org/10.1016/j.energy.2020.118101

Zhu, H., Salyani, M., & Fox, R. D. (2011). A portable scanning system for evaluation of spray deposit distribution. *Computers and Electronics in Agriculture*, *76*(1), 38–43. https://doi.org/10.1016/j.compag.2011.01.003

Żrodowski, Ł., Wróblewski, R., Link to external site, this link will open in a new window, Choma, T., Link to external site, this link will open in a new window, Morończyk, B., Link to external site, this link will open in a new window, Ostrysz, M., Leonowicz, M., Link to external site, this link will open in a new window, Łacisz, W., Błyskun, P., Wróbel, J. S., Link to external site, this link will open in a new window, Cieślak, G., Wysocki, B., Link to external site, this link will open in a new window, Żrodowski, C., & Pomian, K. (2021). Novel Cold Crucible Ultrasonic Atomization Powder Production Method for 3D Printing. *Materials*, *14*(10), 2541. https://doi.org/10.3390/ma14102541

Appendices

Appendix A: Steps to use ImageJ to analyze area and quantity of water droplets on the water sensitive paper

1. Download ImageJ program package from https://imagej.nih.gov/ij/download.html
   a. The package comes with in a zip file, save the unzipped folder in an accessible place
   b. The program does not require an installation wizard, just open the executable (.exe) file in the unzipped folder

 | ☐ Name | Date modified | Type | Size |
   |---|---|---|---|
   | 📁 jre | 10/24/2022 5:39 PM | File folder | |
   | 📁 luts | 10/24/2022 5:39 PM | File folder | |
   | 📁 macros | 10/24/2022 5:39 PM | File folder | |
   | 📁 plugins | 10/24/2022 5:39 PM | File folder | |
   | 📄 ij.jar | 9/10/2022 12:40 PM | JAR File | 2,410 KB |
   | 📄 ImageJ.cfg | 10/24/2022 5:41 PM | CFG File | 1 KB |
   | 📄 ImageJ.exe | 6/28/2015 7:56 PM | Application | 386 KB |

   c. The ImageJ toolbar will look like this:
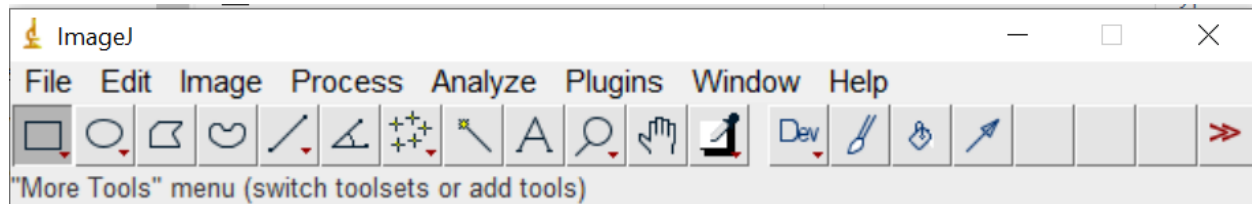
2. Have an image file taken of the water sensitive paper in your computer (and preferably another image file with measurement length references for later in Section 4.a.ii.1)
   a. The program can accept the following file types: GIF, JPEG, BMP, PNG, PGM, FITS, ASCII, DICOM
   b. In the ImageJ program, click on to the "File" button => Click on the "Open" button on the dropdown => Select your desired image file from the opened file explorer window and click the "Open" button
   c. An additional window will open with the chosen picture followed by the pixel dimension, image color range type, and image file size on the top left, as so:
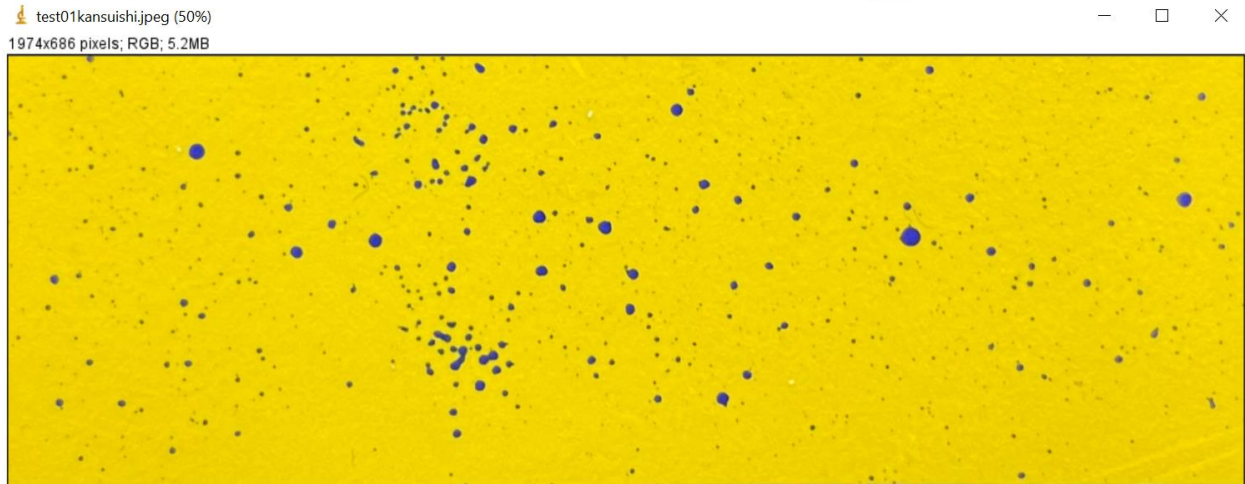
3. To optimize and increase the droplet resolution of the photo for analysis of droplet area and quantity, we will alter the photo to 8-bit grey scale and use black/white pixelation

    a. In the ImageJ program toolbar, click on "Image" => mouse over the "Type" tab on the dropdown => select the "8-bit" option on the next popup dropdown. This will change our image file into an 8-bit greyscale.
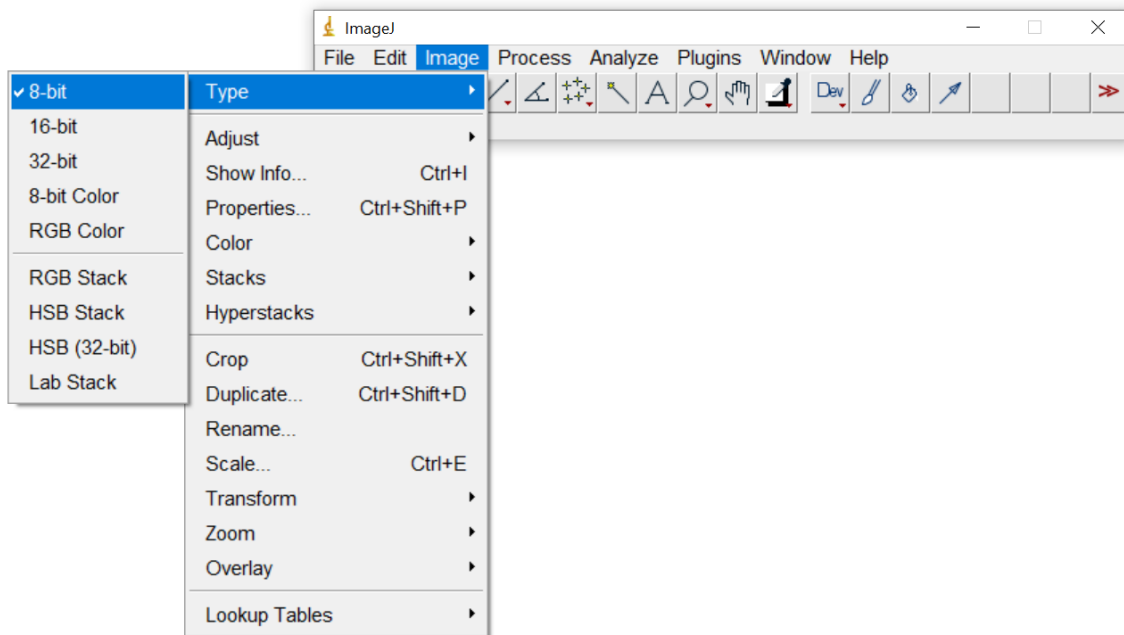

    b. Click on "Image" again => mouse over the "Adjust" tab on the dropdown => select the "Threshold…" option in the next popup dropdown.
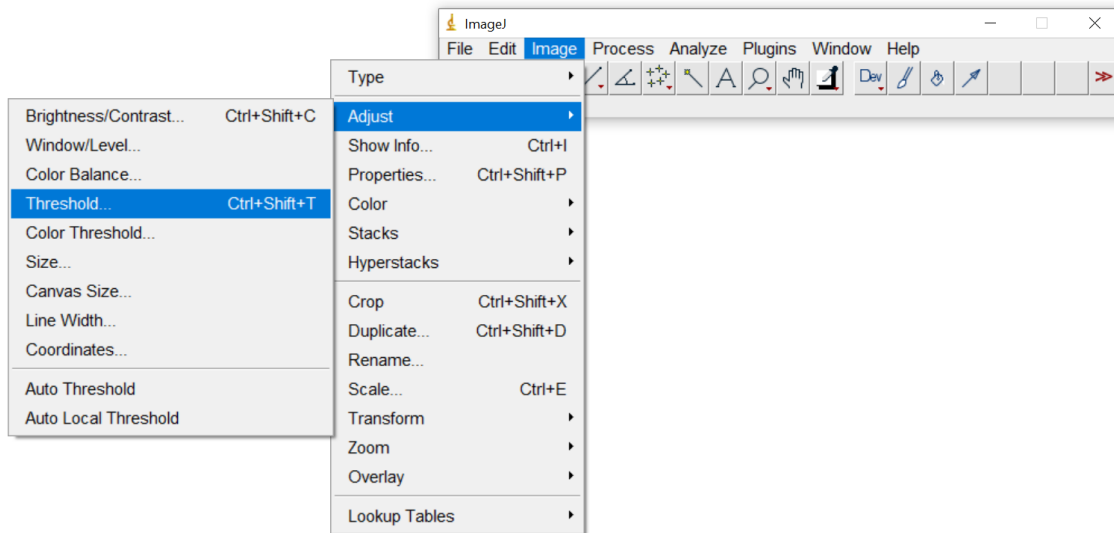
i.   A threshold popup window will open. In this window, switch the center two dropdown list to "Default" and "B&W" if they haven't been changed yet.

ii. Uncheck the checkbox next to the "Dark background" option

iii. Adjust the upper and lower threshold using the upper center two sliders until you get the desired resolution and visibility for the given droplets on the water sensitive paper (where droplet complete diameter is in view).
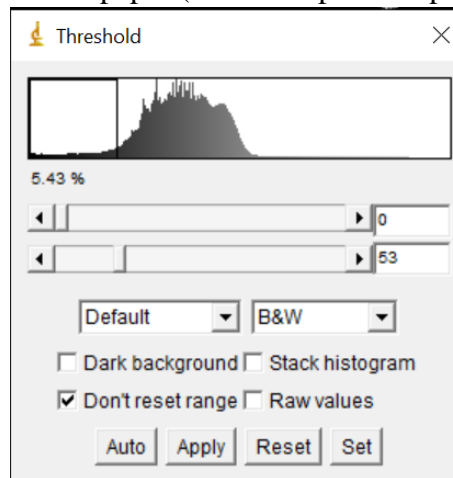
iv. To confirm your choices, press the "Apply" button. The resulting image file should look like this:
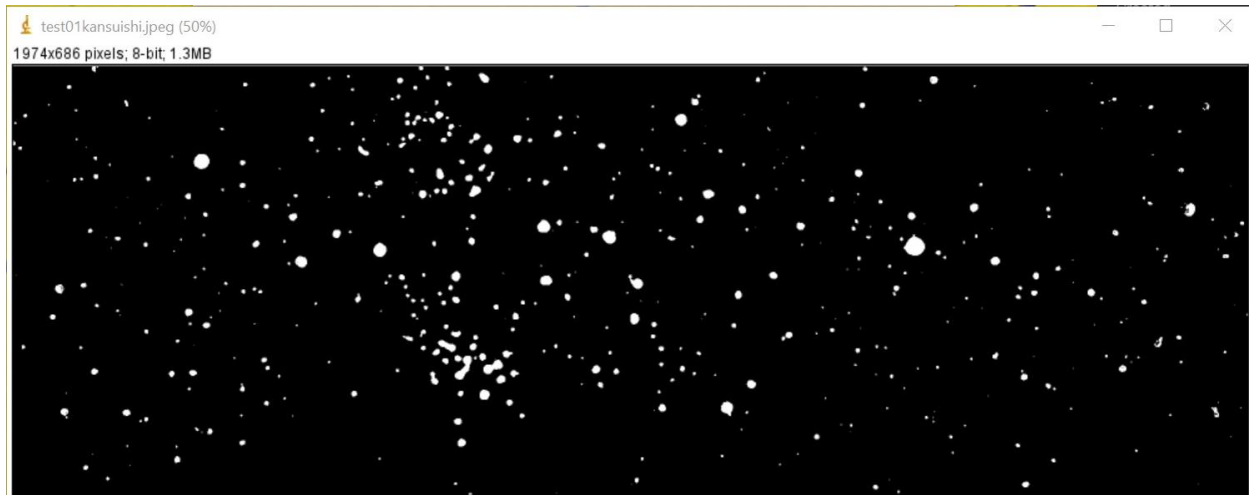
c. During this time, if you would like, you can save your converted image as a separate file by clicking on the "File" button from the toolbar window, mousing over the "Save As…" button on the dropdown => clicking on the desired file type to save as from the popup dropdown list (Tiff, Jpeg, etc.) => naming and selecting folder to save file from the popup explorer window
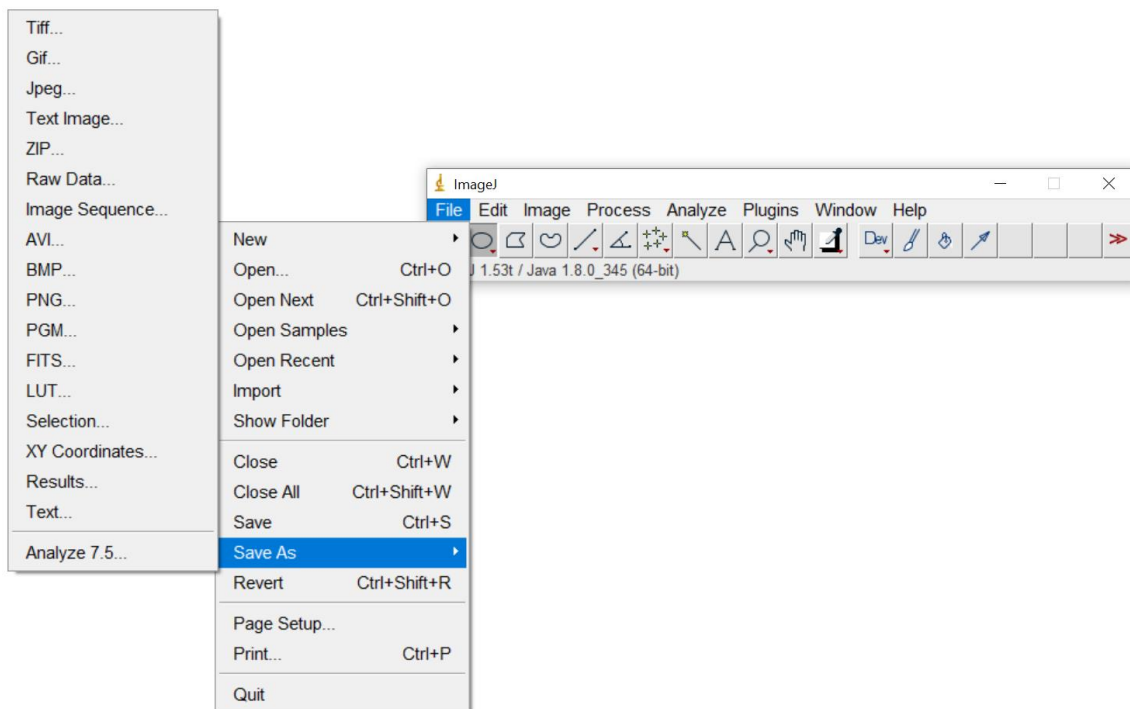
4. We will then apply a measurement scale to the picture to let ImageJ analyze droplet area later with the chosen real-world measurement values.
    a. To set the measurement scale, go to the "Analyze" dropdown => click on the "Set Scale…" button in the dropdown
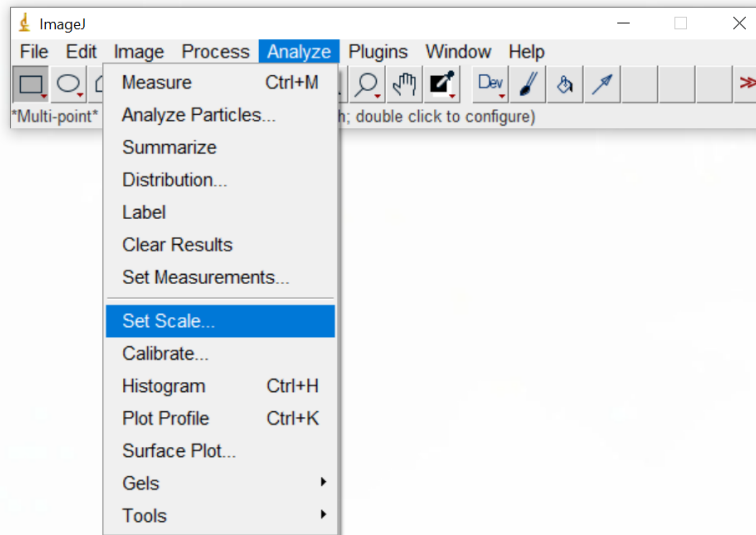
    i.   Use a frame of reference with the total pixel length of an object in the photo and the real-world measurement length. Insert this information in the "Set Scale" window towards the right text boxes next to "Distance in pixels:" and "Known distance:". Leaving the text box to the right of "Pixel aspect ratio:" as "1.0" is fine as most devices output images with square, or 1:1, pixels. Fill in the text box on the right of "Unit of length:" with the measurement unit chosen to measure the object, this will allow ImageJ to label the reference measurement correctly if needed.

   ii.   Check the box next to "Global" option in the window to allow the measurement scale to be use across different image files => click the "OK" button to confirm the scale adjustment.
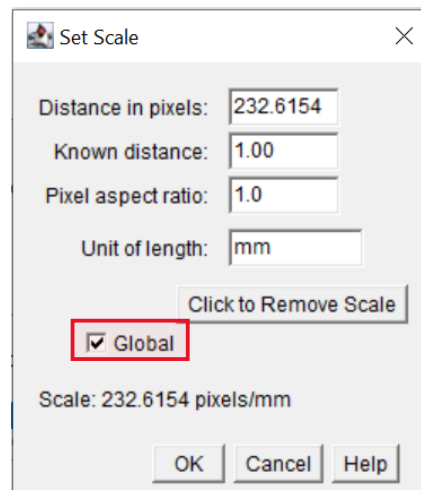
    1.   If you are not sure what the pixel distance for the measurement value is exactly, ImageJ allows you to take the measurement with
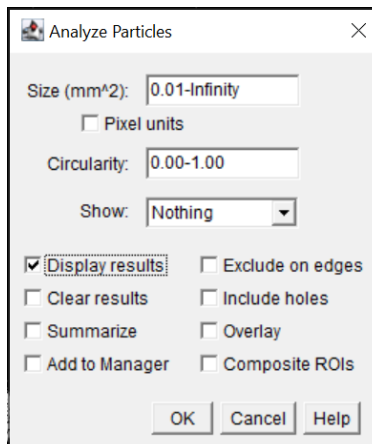
the dropdown "Straight" tool (the grey highlighted square block button in the screenshot below). Just open another picture file with the desired object length to be measured => line up the created straight line on the desired length on the object (as shown in the red box below) => open the "Set Scale" window like before. The "Distance in pixels:" right-side text box should be highlighted with the pixel length of the created straight line. Next, fill in the value of the 'known distance:" in the textbox with the correlating real world length for the chosen length of the "Straight" tool as explained before in section "4i" => check the "Global" checkbox => click on the "OK" button below.
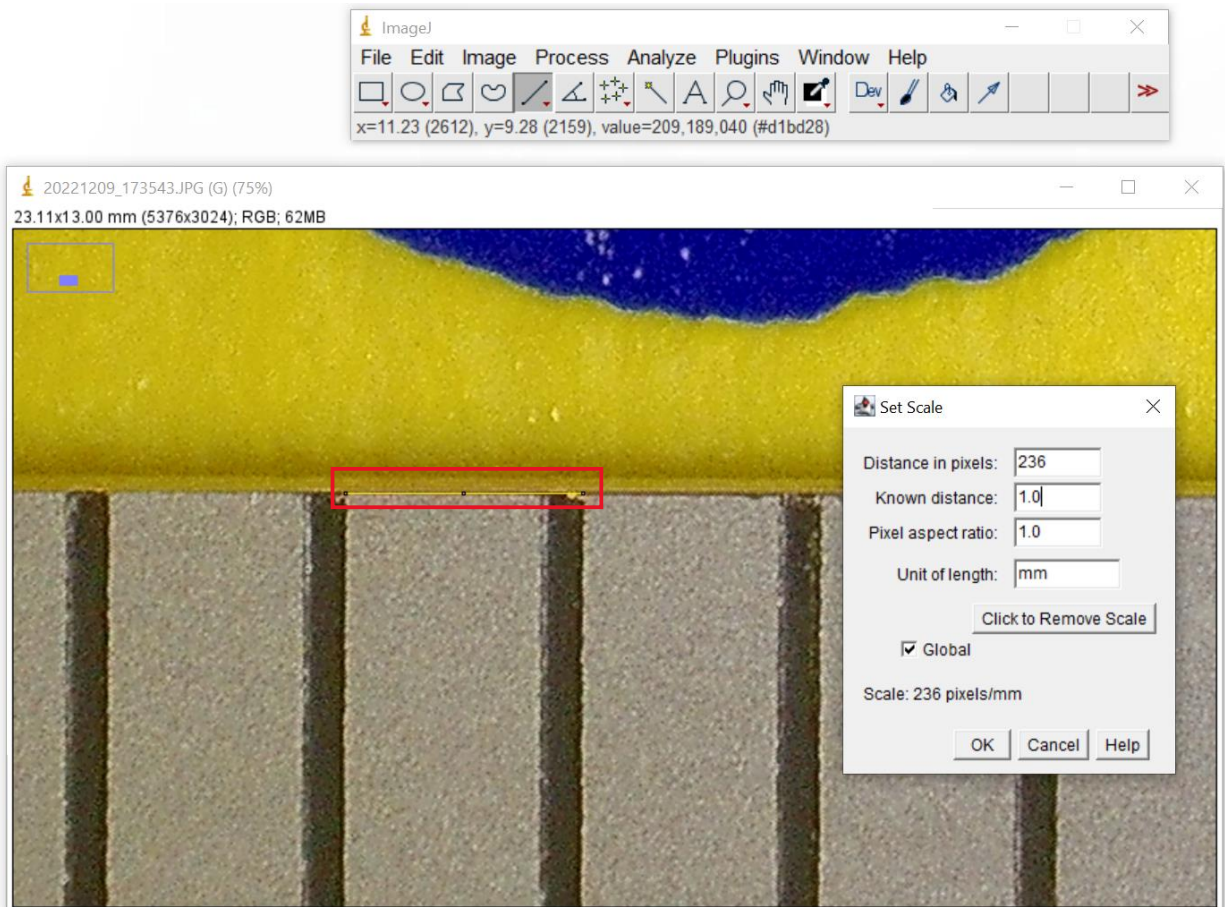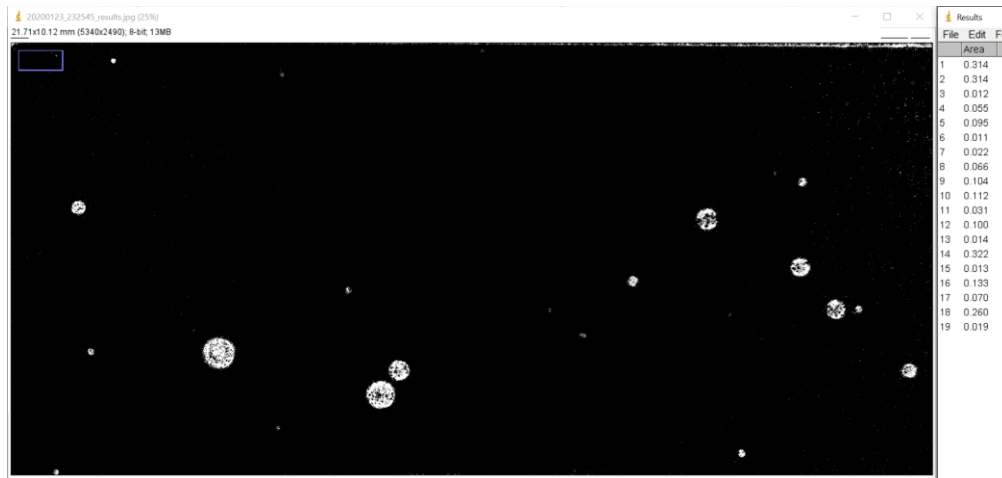

b. To tell ImageJ what you want to analyze, we will open the "Set Measurement" window
    i. For our specific analysis requirement in this experiment, we will only require knowledge of the particle's measured area. As so, leave only the checkbox to the left of the "Area" selection filled with a checkmark.
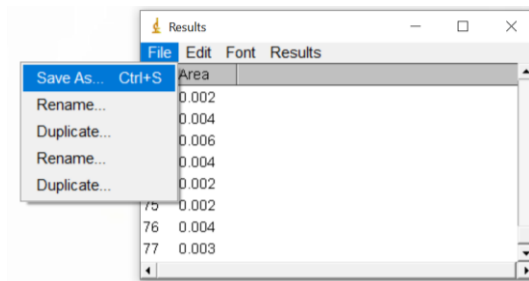
Set Measurements ×

☑ Area ☐ Mean gray value
☐ Standard deviation ☐ Modal gray value
☐ Min & max gray value ☐ Centroid
☐ Center of mass ☐ Perimeter
☐ Bounding rectangle ☐ Fit ellipse
☐ Shape descriptors ☐ Feret's diameter
☐ Integrated density ☐ Median
☐ Skewness ☐ Kurtosis
☐ Area fraction ☐ Stack position

☐ Limit to threshold ☐ Display label
☐ Invert Y coordinates ☐ Scientific notation
☐ Add to overlay ☐ NaN empty cells

Redirect to: None ▾
Decimal places (0-9): 3

OK Cancel Help

5. To analyze the photo, we will open the "Analyze Particles" window
   a. The size of the particle is determined by the measured area of the displaced droplet impressions. Particle units are based on the chosen unit scale. Adjust the range on the text box next to the size counter with the given syntax "lower range – upper range" to an estimated value for the given droplets => similarly adjust the "circularity" range To measure any object with an area above the lower range value, just replace the numerical value with the term 'Infinity'. Click "OK" below the window to begin the analysis.
      i. A lower range value is recommended to be set since the Analyze Particles function will calculate particles produced due to image noise as well. For our experiment, the lower range of 0.00196mm^2 for size and 0.05 for circularity was chosen in correlation to the accuracy tolerance of our water sensitive paper droplet recording apparatus. Feel free to repeat this process, adjusting the circularity range until the results output are satisfactory

Analyze Particles ×

Size (mm^2): 0.01-Infinity
    ☐ Pixel units
Circularity: 0.00-1.00
Show: Nothing ▾

☑ Display results ☐ Exclude on edges
☐ Clear results ☐ Include holes
☐ Summarize ☐ Overlay
☐ Add to Manager ☐ Composite ROIs

OK Cancel Help

b. The results output and the transformed image should be visible as shown below:


c. Once the results are outputted, you can save the results as a .CSV file by clicking on the "File" button on the "results" window toolbar => clicking on the "Save as…" button from the dropdown => naming and selecting a save location for the .CSV file from the popup explorer window.

6. To perform another calculation with another image, complete the following tasks from section 2-5 again. If the measurement scaling used in calculating the following image is the same as with the previous image, feel free to skip section 4. Section 3 can be repeated if the results from section 5 aren't satisfactory even with adjustments within the Analyze Particle window (i.e. incorrect/unexpected particle count).

Additional Tools:

<u>Crop</u> – Use the selection tools in the ImageJ main toolbar (the square box buttons underneath the dropdown option buttons) to select an area you want to retain, then select the "image" button on the ImageJ toolbar and select "crop" on the dropdown to activate the tool. All elements within the perimeter of the selection tool path created beforehand will be kept, all elements outside will be removed. ImageJ's photo window will resize after this process in correlation to the current pixel resolution of the image.
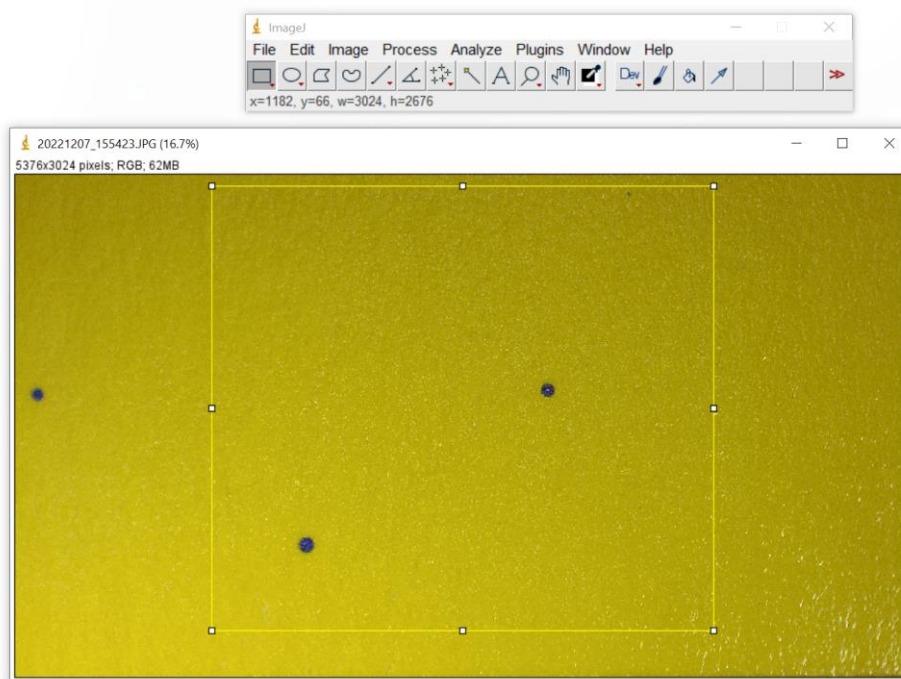
<u>Fill/ Clear</u> – As shown below in the two sample images, these two functions allow the user to clear out sections of a transformed or untransformed image that is selected previously using a selection tool from the toolbox. This can be helpful when you want to mask or clean up resulting noise particles or objects you want Analyze Particle function to ignore after a threshold transformation. To use these tools, start by selecting a selection tool from the ImageJ toolbar => select an area that you would like to mask or clear out with the selection tool => mouse over to

the "Edit" button on the toolbar => select either "Fill" or "Clear" button depending on the

function you want to use.

- Usually, the "Fill" function will fill the selected spot with white, which the analyze particle function will pick up as particle area. This is helpful with cleaning up obfuscated particle which the threshold transformation cannot completely recognize from the photo.
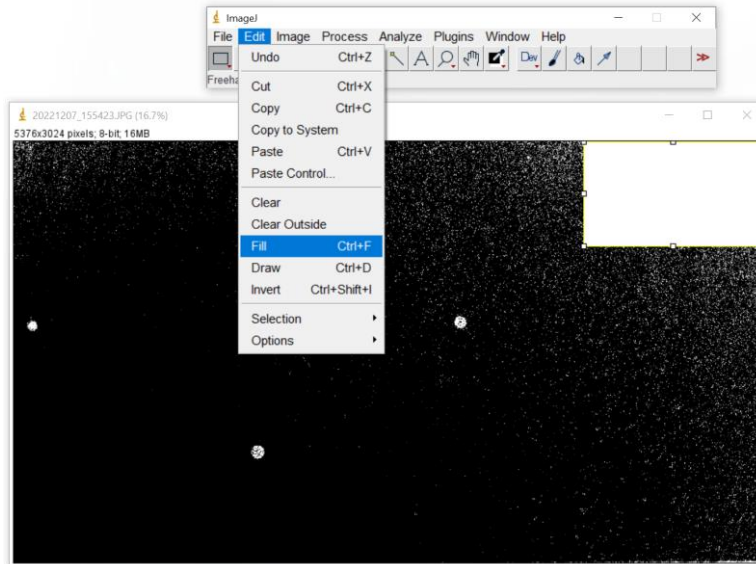
- The "Clear" function will do the opposite to the fill function, filling the enclosed space with black which the Analyze Particle function ignores. This can be used to mask out sections of noise particles after a threshold transformation, which usually generate due to uneven lighting in the photo.